https://ntrs.nasa.gov/search.jsp?R=20170011457 2019-05-01T02:35:14+00:00Z

Chemical Mechanisms and their Applications in the Goddard Earth Observing System (GEOS) Earth System Model

J. Eric Nielsen[3,1], Steven Pawson[1], Andrea Molod[1], Benjamin Auer[3,1], Arlindo M. da Silva[1], Anne R. Douglass[2], Bryan Duncan[2], Qing Liang[4,2], Michael Manyin[3,2], Luke D. Oman[2], William Putman[1], Susan E. Strahan[4,2], and Krzysztof Wargan[3,1]

[1]Global Modeling and Assimilation Office, NASA Goddard Space Flight Center, Greenbelt, Maryland, USA.
[2]Atmospheric Chemistry and Dynamics Laboratory, NASA Goddard Space Flight Center, Greenbelt, Maryland, USA.
[3]Science Systems and Applications, Inc., Lanham, Maryland, USA.
[4]Goddard Earth Science and Technology Center, Universities Space Research Association, Columbia, Maryland, USA.

Key Points:

- The GEOS Earth System Model's architecture is based on ESMF and the GMAO's middleware layer called MAPL.
- GEOS uses a common code base of interchangeable chemical components for data assimilation, forecasting, and research.
- GEOS is applied to atmospheric chemistry topics ranging from diurnal air quality variations to climate change.

Corresponding author: J. Eric Nielsen, `jon.e.nielsen@nasa.gov`

Abstract

NASA's Goddard Earth Observing System (GEOS) Earth System Model (ESM) is a modular, general circulation model (GCM) and data assimilation system (DAS) that is used to simulate and study the coupled dynamics, physics, chemistry, and biology of our planet. GEOS is developed by the Global Modeling and Assimilation Office (GMAO) at NASA Goddard Space Flight Center. It generates near-real-time analyzed data products, reanalyses, and weather and seasonal forecasts to support research targeted to understanding interactions among Earth-System processes. For chemistry, our efforts are focused on ozone and its influence on the state of the atmosphere and oceans, and on trace-gas data assimilation and global forecasting at mesoscale discretization. Several chemistry and aerosol modules are coupled to the GCM, which enables GEOS to address topics pertinent to NASA's Earth Science Mission.

This manuscript describes the atmospheric chemistry components of GEOS and provides an overview of its Earth System Modeling Framework (ESMF)-based software infrastructure, which promotes a rich spectrum of feedbacks that influence circulation and climate, and impact human and ecosystem health. We detail how GEOS allows model users to select chemical mechanisms and emission scenarios at run time, establish the extent to which the aerosol and chemical components communicate, and decide whether either or both influence the radiative transfer calculations. A variety of resolutions facilitates research on spatial and temporal scales relevant to problems ranging from hourly changes in air quality to trace gas trends in a changing climate. Samples of recent GEOS chemistry applications are provided.

1 Introduction

Among the most important factors influencing the long-term evolution of the atmosphere are feedbacks between its chemical composition and an array of other physical processes that include, for example, radiative transfer, clouds, and precipitation. The desire to quantify the influence of feedbacks and to identify those that are most important fundamentally motivates our desire to understand atmospheric chemistry and air pollution. To study these complicated and often nonlinear interactions, atmospheric scientists have developed general circulation models of the atmosphere that today are capable of utilizing thousands of processors to accommodate global spatial discretizations down to 10 km or less in the horizontal and tens to hundreds of meters in the vertical. At NASA's Goddard Space Flight Center (GSFC), the Global Modeling and Assimilation Office (GMAO) in partnership with the Atmospheric Chemistry and Dynamics Laboratory (ACDL) instituted a project approximately a decade ago to integrate photochemical mechanisms of increasing complexity into GSFC's atmospheric general circulation model (AGCM), the Goddard Earth Observing System (GEOS) Model. The initial objective was to accurately simulate ozone evolution in a changing environment. *Pawson et al.* [2008] described the first version of the coupled model, for which a detailed stratospheric chemistry (StratChem) module [*Douglass and Kawa*, 1999; *Considine et al.*, 2000] was developed. It was used to examine long-term impacts of the growth and decline of chlorofluorocarbons (CFCs) on the stratosphere's ozone layer [*Stolarski et al.*, 2010] and to study the influence of the Antarctic ozone hole on tropospheric circulation [*Perlwitz et al.*, 2008]. Through participation in the Chemistry-Climate Model (CCM) Validation Activity (CCMVal) [*Eyring et al.*, 2006], GEOS became established as one of the leading CCMs based on several objective, performance-based metrics [*Waugh and Eyring*, 2008; *Eyring et al.*, 2010]. Other CCM projects in the United States, Europe, and Japan are detailed in the above references and in documents from the Stratospheric Processes and their Role in Climate (SPARC) initiative of the World Climate Research Programme (WCRP).

Successes with GEOS in studying the ozone layer and its relation to climate motivated efforts to enhance its ability to address other topics in chemistry and transport important to NASA's Earth Science Mission [*Stolarski et al.*, 2006; *Douglass et al.*, 2014; *Oman*

and Douglass, 2014]. Substantial improvements to the atmospheric physical parameterizations [*Molod et al.*, 2015] were supplemented by introducing aerosol modules [*Colarco et al.*, 2010] and by acquiring modern, highly-resolved emissions inventories. The dynamical core has been upgraded so that integrations can be performed on cubed-sphere grids [*Putman and Lin*, 2007], which are more scalable and more accurately represent transport than longitude-latitude grids, especially over the poles. The "stratosphere-troposphere chemical mechanism" developed by the Global Modeling Initiative [*Duncan et al.*, 2007], hereafter GMI-STM, was added along with software that enables run-time selection of an experiment's configuration and discretization. The ability to adapt to and take advantage of ever-evolving, massively parallel computing architectures and to execute GEOS in multiple environments is reflected in the increasing complexity of its software, whose foundation in the Earth System Modeling Framework (ESMF) [*Hill et al.*, 2004] and the Modeling Analysis and Prediction Layer (MAPL) [*Suarez et al.*, 2007] promotes flexibility and extensibility. In the current era of rapidly evolving trends in emissions, the emphasis of GEOS chemistry-based research is evolving to include modeling and forecasting tropospheric pollution and air quality, assimilating trace gases, and creating datasets to support observing systems simulations. Each of these topics is driving rapidly expanding resource requirements to accommodate more comprehensive chemical mechanisms than those currently implemented and to enable integrations on scales fine enough to resolve trace constituent gradients near the ground.

The GMAO's model development and validation efforts seek to maximize the use of trace-gas information contained in retrievals and radiances from NASA's Earth Observation System (EOS) and subsequent satellites. Since the 1970s NASA has been mandated to monitor stratospheric ozone, for which global analyses are generated. The GMAO's data assimilation system (DAS) first relied on a series of Solar Backscattered Ultraviolet (SBUV) radiation and Total Ozone Mapping Spectrometers (TOMS) [*Heath et al.*, 1975]. Since 2004, these observations have been extended and enhanced by the launch and operation of the EOS Aura platform. On board Aura are the Microwave Limb Sounder (MLS) [*Waters et al.*, 2006], which retrieves ozone profiles in the stratosphere and the upper troposphere down to 261 hectopascals (hPa), and the Ozone Monitoring Instrument (OMI) [*Levelt et al.*, 2006], which provides total column measurements. Information from both instruments is being used by the GMAO to demonstrate the accuracy of simulated springtime Arctic ozone depletion in GEOS when it is configured with StratChem coupled to the GEOS DAS. OMI also measures column nitrogen dioxide (NO_2), which has been used to quantify near-surface pollution and to measure trends during the Aura period [*Duncan et al.*, 2016; *Lamsal et al.*, 2015]. As we endeavor to upgrade the aerosol and chemical mechanisms and couple each to the ocean biogeochemistry, land-surface, and dynamic vegetation components, observations from the above platforms and others will be critical for constraining model performance and guiding improvements. *Flemming et al.* [2017] describe similar efforts to combine trace constituent assimilation with chemical and aerosol modeling at the European Centre for Medium-Range Weather Forecasts.

This manuscript provides documentation of the current version of GEOS from a chemical perspective. Section 2 begins by summarizing the contents of the dynamical core and the physical parameterizations in the AGCM. It then provides a technical description of the chemical components. With the context of the basic elements in place, Section 3 introduces key aspects of GEOS's ESMF-based infrastructure beginning with a description of the GMAO's middleware layer that simplifies software development. It then describes functional units of the hierarchy, and how they fit into the overall structure of the model and promote flexibility in configuring experiments. Section 3 concludes by illustrating and describing the coupling between the chemical components and their connections to the AGCM. Section 4 offers examples that highlight the diverse capabilities of GEOS chemistry. We close by discussing near-term, chemically-oriented GEOS development efforts in Section 5.

2 Model Description

This section presents a summary of the building blocks of GEOS with an emphasis on the chemistry components. As summarized below, GEOS has been substantially updated since the version described by *Rienecker et al.* [2008], most importantly in the moist processes and turbulent diffusion components [*Molod et al.*, 2012, 2015].

2.1 Dynamics

Large-scale transport and dynamics in GEOS is computed by an adaptation of the flux-form semi-Lagrangian (FFSL) finite-volume (FV) dynamics of *Lin* [2004] for a cubed sphere horizontal discretization [*Putman and Lin*, 2007]. The FFSL scheme [*Lin and Rood*, 1996, 1997] is motivated by requirements for accurate and consistent scalar transport of trace constituents, mass, and potential vorticity. FFSL is by design mass conserving, and its local discretization enables it to maintain sharp gradients. FV features a conservative mapping from floating Lagrangian control volumes to GEOS's Eulerian, terrain-following coordinate. GEOS also contains a separate stand-alone FV advection module outside of the "dynamical core" for use in off-line experiments. In multiple-model comparison exercises where transport statistics are objectively measured against observations, the FV dynamical core is known to perform well. For example, in integrations spanning several decades, the transport of long-lived constituents in the stratosphere indicates that the residual mean meridional circulation is accurately simulated [*Pawson et al.*, 2007; *Eyring et al.*, 2006, 2007].

The motivation for the transition to the cubed sphere grid is twofold. The first is computational stability. Longitude-latitude grids are inherently unstable near the poles because cell area diminishes due to the convergence of meridians. The cubed sphere's grid is quasi-uniform over the entire globe, which eliminates the need to apply a filter over the poles to maintain stability. In addition, because cell areas over the broader polar cap regions are similar to those near the Equator, the cubed sphere is especially advantageous during intervals of strong cross-polar flow such as sudden stratospheric warmings. The discontinuities at the edges and corners of the cube's six faces present computational challenges. However, *Putman and Lin* [2007] show that as moving vortices pass over the corners, error growth rates are comparable to those in the original longitude-latitude implementations, and they decline as resolution is enhanced. The second motivation is scalability. The grid facilitates two-dimensional domain decomposition on distributed computing architectures, and enables implementation of a completely general algorithm for determining and allocating processor layouts that is extensible to ultra-high resolutions. The cubed sphere is thus particularly well suited for explicitly resolving previously parameterized processes such as convection [*Putman and Suarez*, 2011].

GEOS's vertical discretization is a generalized hybrid sigma-pressure vertical coordinate [*Simmons and Burridge*, 1981]. The current standard configuration is composed of 72 layers, which are terrain-following at the ground and throughout the lower troposphere. As altitude increases, the layers gradually become isobaric, with the transition completed at approximately 12 km (176 hPa). Layer number 1 is at the model's lid, which lies at 0.01 hPa (approximately 80 km), and layer 72 lies on the ground. Vertical discretization is finest in the lower troposphere, where layer thicknesses are as thin as 60 m at the ground. The layers become thicker with elevation in the troposphere and are approximately 2 km deep in the upper stratosphere and mesosphere.

2.2 Physics

GEOS physics includes parameterizations for convection, large scale precipitation and cloud cover, longwave and shortwave radiation, turbulence, gravity wave drag, and land surface processes. Convection is parameterized using the Relaxed Arakawa-Schubert scheme [*Moorthi and Suarez*, 1992], which contains an updraft-only cloud model and a quasi-equilibrium

closure. The frequency and intensity of deep convection is governed by a stochastic Tokioka-type trigger function [*Tokioka et al.*, 1988] as suggested by *Bacmeister and Stephens* [2011]. Prognostic cloud cover and cloud water and ice are determined by the single moment parameterization of *Bacmeister et al.* [2006], which includes large scale condensation, evaporation, autoconversion and accretion of cloud water and ice, sedimentation of cloud ice, and re-evaporation of falling precipitation. The probability distribution function (PDF) for total water that governs the condensation and evaporation processes is described by *Molod* [2012]. GEOS also has the option to instead execute a two-moment cloud microphysics module, which improves the simulation of clouds and condensate in many regions [*Barahona et al.*, 2014].

Longwave radiative processes are described by *Chou and Suarez* [1994], and include absorption due to cloud water, water vapor, aerosols, carbon dioxide (CO_2), ozone (O_3), nitrous oxide (N_2O), methane (CH_4), chlorofluorocarbons CFC-11 and CFC-12, and hydroclorofluorocarbon HCFC-22. Shortwave radiative transfer is from *Chou* [1990, 1992], and includes absorption by water vapor, cloud water, O_3, CO_2, molecular oxygen (O_2), and aerosols, and scattering by cloud water and aerosols. The global concentration of CO_2 is specified from *Meinshausen et al.* [2011], and the shortwave flux reduction due to O_2 is derived from a simple function applied to the insolation. The remaining eight constituents listed above are simulated and prognostic, as are the aerosols. Their three-dimensional, time-dependent fields are imported into the radiation components, which facilitates chemistry's influence on the dynamics via thermal forcing. The rapid radiative transfer model for GCMs (RRTMG) [*Iacono et al.*, 2000] is also available in GEOS.

The turbulence parameterization is based on the Lock scheme [*Lock et al.*, 2000] interfaced with the Richardson-number based algorithm of *Louis and Geleyn* [1982]. The former includes a representation of non-local mixing driven by both surface fluxes and cloud-top processes in unstable layers, either coupled to or decoupled from the surface. It was extended in GEOS to include moist heating and entrainment in the unstable surface parcel calculations which determine the depth of unstable layers. The latter is a first-order local scheme, and its effect is mostly felt just above the surface layer and in regions of shear-generated turbulence. The turbulent length scale that governs its behavior is a function of the planetary boundary layer height at the previous time step [*Molod et al.*, 2015], which is diagnosed based on the profile of eddy diffusivity over the ocean and on a bulk Richardson number threshold over land [*McGrath-Spangler and Molod*, 2014]. The Monin-Obukhov surface layer parameterization is described by *Helfand and Schubert* [1995] and includes the effects of a viscous sublayer for heat and moisture transport over all surfaces except land. Ocean surface roughness is determined by a blend of the algorithms of *Large and Pond* [1981] and *Kondo* [1975], modified in the midrange wind regime according to *Garfinkel et al.* [2011] and in the high wind regime according to *Molod et al.* [2013]. The gravity wave drag parameterization computes momentum and heat deposition due to orographic [*McFarlane*, 1987] and nonorographic [*Garcia and Boville*, 1994] waves. The background drag profile that generates an internal quasi-biennial oscillation (QBO) is described by *Molod et al.* [2015]. They demonstrate that downward propagation of the zonal wind anomalies is realistic, but phase speeds are slower and amplitudes are larger than those observed.

2.3 Chemical Mechanisms for Atmospheric Gases

GEOS has several chemical components of varying complexity for the simulation of atmospheric gases. Section 2.3.1 describes the "parameterized chemistry" (PCHEM) module, which executes quickly, is the component that provides radiatively active trace gases in the GMAO's data assimilation system (DAS) production environment, and can be used in simulations and studies that are not specifically targeted at complex chemistry. Section 2.3.2 summarizes the "stratospheric chemistry" (StratChem) package, which provides an economical and accurate mechanism for studies of O_3 depletion and recovery and of the influence of O_3-depleting substances (ODSs) and greenhouse gases (GHGs) on the climate of the middle

atmosphere. A comprehensive "troposphere-stratosphere chemistry" mechanism, the subject of Section 2.3.3, is available for detailed chemical process studies on diurnal to multi-decadal time scales. It is currently too expensive to be employed in DAS operations, but has assumed an important role in the GMAO's chemistry-climate simulations. It is also used in short-term, high-resolution simulations that demonstrate GEOS can generate chemical signatures of important meteorological phenomena such as regional and intercontinental transport, tropical storms, and stratospheric intrusions. Section 2.3.4 describes a new, efficient CH_4-CO-OH module [*Elshorbany et al.*, 2016] that has recently been developed to investigate the long-term climate impacts of CH_4 emissions with a parameterization that can quickly produce ensembles of century-length simulations. Section 2.3.5 details the "passive tracer" component, which can be run in tandem with any of the other chemistry components. It instantiates a suite of idealized and realistic tracers that can be used for the diagnosis of GEOS's circulation on both short and long time scales.

2.3.1 Parameterized Chemistry

GEOS's most rapidly executed chemical component parameterizes the stratospheric concentrations of the important radiatively active trace gases: O_3, CH_4, N_2O, two chlorofluorocarbons, CFC-11 and CFC-12, hydroclorofluorocarbon HCFC-22, and water vapor (H_2O), for the purpose of establishing heating and cooling rates in the stratosphere. Parameterized chemistry (PCHEM) has two configurations. The first is based on linearized production and loss where a constituent, x, is governed by

$$x(t + dt) = (x^* + Pdt)/(1 + Ldt).$$

P is the production rate, L is the loss frequency, t is time, and x^* is the state produced by transport and turbulence. The coefficients P and L are monthly averages derived from an integration of the GSFC two-dimensional chemistry and transport model [*Fleming et al.*, 2011] to steady state with modern boundary conditions. This is the configuration that is used in the GMAO's DAS forward processing, in the generation of our reanalyses, the Modern-Era Retrospective Analysis for Research and Applications (MERRA) [*Rienecker et al.*, 2011] and MERRA-2 [*Gelaro et al.*, 2017], and in operational and seasonal forecasting.

In the second configuration, PCHEM relaxes the concentrations of the seven gases (H_2O only above the tropopause) to a prescribed set of monthly zonal averages with a time constant for each gas that is declared at run time and applied globally. This allows the gases to be transported by the large-scale dynamics and by sub-grid-scale convection and turbulence without substantially drifting from their prescriptions. For a long-lived gas like CH_4 in the stratosphere, experience dictates that time constants between about three and ten days allow the isopleths to align with potential vorticity contours on horizontal projections.

In practice, PCHEM's linearized mode is applied only to present-day simulations. But its relaxation mode can be used to represent past or future stratospheres by customization of the zonally averaged monthly mean relaxation fields. For example, the GMAO's retrospective climate investigations [*Schubert et al.*, 2014] use a time-dependent climatology that is generated by a multiple-step process. First, five-year running averages of monthly zonal means are computed from a 1950-2010 simulation that used an older version of GEOS. Bias correction of N_2O, CH_4, CFC-11, CFC-12, and HCFC-22 is accomplished by scaling each to their respective surface mixing ratios specified by the fifth phase of the Coupled Model Intercomparison Project (CMIP5) historic midyear concentrations [*Meinshausen et al.*, 2011]. The 1951-1955 monthly averages for N_2O and CH_4 are then copied to each year back to 1870 after scaling them to the the CMIP5 concentrations for each respective year. Stratospheric H_2O is also projected back to 1870 based on the twice the change in CMIP5 surface CH_4 concentration lagged by five years, the assumed age-of-air (AOA). Finally, for O_3, monthly averages from 1870-2005 [*Cionni et al.*, 2011] were downloaded from the Earth System Grid Gateway and converted to zonal means.

2.3.2 Stratospheric Chemical Mechanism

The first reactive gases chemistry component in GEOS was originally developed in the 1990s for multi-decadal simulations of stratospheric O_3 with a chemistry and transport model (CTM, See Section 4, paragraph 1 for an example.). Called StratChem, results from early versions are described by *Kawa et al.* [1995], *Douglass et al.* [1997], *Douglass and Kawa* [1999], *Kinnison et al.* [2001], and *Douglass et al.* [2004]. These studies validated StratChem's performance in configurations that did not allow chemical feedback to the dynamics through radiative forcing, but demonstrated that the mechanism was capable of reproducing realistic polar O_3 loss prior to implementing it in GEOS. Using GEOS, *Pawson et al.* [2008] evaluate O_3 and temperature fields from simulations spanning 1980 through 2000 by comparing them to observations, and demonstrate the importance of radiative feedback. *Perlwitz et al.* [2008] extended simulations to 2100 to show how the growth and decay of the Antarctic O_3 hole affects circulation patterns in the southern hemisphere and influences Antarctic surface climate change.

The current equation set consists of 125 thermal and 35 photolytic reactions. StratChem utilizes a family approach that includes O_x [$O_3 + O(^1D) + O(^3P)$], NO_x ($NO + NO_2 + NO_3$), ClO_x ($ClO + OClO + 2Cl_2O_2$), and Br_x ($Br + BrO$). The families are transported. Their members are inferred through steady-state partitioning during daylight hours (but not at night) as the solver progresses sequentially through the families first with an estimator step followed by a corrector step. In the mesosphere, five photolysis reactions acting on O_2, nitric oxide (NO), and CH_4 are added in order to balance the H_2O and CH_4 budgets. That is, CH_4 photolysis yields H_2O and is necessary to simulate the observed moistening of the upper atmosphere. Heterogeneous chemical reactions on stratospheric sulfate aerosol as well as Type 1 and Type 2 polar stratospheric clouds (PSCs) are treated as in *Considine et al.* [2000, 2003]. In the troposphere, O_3 is relaxed to a zonally averaged climatology constructed from observations. Similarly, the three-dimensional hydroxyl radical (OH) concentration in the troposphere is borrowed from *Spivakovsky et al.* [2000]. OH acts to restrain the growth of the surface source gases methyl chloroform (CH_3CCl_3), methyl chloride (CH_3Cl), methyl bromide (CH_3Br), HCFC, and CH_4.

Improvements to StratChem in recent releases of GEOS are described by *Oman and Douglass* [2014]. These include extending the transition from day- to night-time chemistry from 90° to 94° solar zenith angle, prescribing observed stratospheric sulfate surface area densities [*Eyring et al.*, 2013], updating the GHG concentrations to Representative Concentration Pathway (RCP) 6.0 [*Meinshausen et al.*, 2011], and adding 5 parts per trillion (pptv) to the CH_3Br surface mixing ratio to account for short-lived brominated species. In addition, *Aquila et al.* [2013] coupled sulfate aerosols from the Goddard Chemistry Aerosol Radiation and Transport (GOCART) component [*Chin et al.*, 2002; *Colarco et al.*, 2010] to StratChem in order to simulate volcano-induced perturbations to stratospheric trace constituents.

Section 4.3 illustrates a new application GEOS with StratChem. It shows how forecasts of the areal coverage of the Antarctic O_3 hole are significantly improved when StratChem replaces PCHEM in the DAS.

2.3.3 Stratosphere-Troposphere Mechanism

The first comprehensive stratosphere-troposphere chemical component in GEOS is the GMI-STM [*Duncan et al.*, 2007], which merges Lawrence Livermore National Laboratory's (LLNL) mechanism developed for the stratospheric version of the GMI model [*Douglass et al.*, 2004] with the existing version of the tropospheric chemical mechanism developed for Harvard University's GEOS-Chem tropospheric chemistry and transport model (CTM) [*Horowitz et al.*, 1998; *Bey et al.*, 2001] with updated photochemical data. The LLNL code was selected in lieu of StratChem since the former contains the infrastructure to support adding the stratospheric equation set to GEOS-Chem's SMVGEAR-II [*Jacobson*, 1995] solver. GMI-STM includes 71 transported species, 50 short-lived non-transported species,

Table 1. VOCs, CO, and NO from biomass burning in 2012. Source: Quick Fire Emission Dataset (QFED) v2.4r6. Daily inventories at 5/16°x1/4°

Species	Tg yr^{-1}	Species	Tg yr^{-1}
Acetaldehyde	2.7	Formaldehyde	3.4
C4,5 alkanes	0.19	Methane	16.8
Ethane	2.5	Carbon monoxide	395
Propene	1.78	Methylethylketone	1.6
Propane	0.61	Nitric oxide	18.2

Table 2. CO and NO from combustion of fuel. Source: Emission Database for Global Atmospheric Research (EDGAR) v4.2 with transportation sector emissions from v4.1. Monthly inventories at 5/16°x1/4°

Species and Source	Tg yr^{-1}	Species and Source	Tg yr^{-1}
CO fossil fuel	267	NO other fossil fuel	27.9
CO biofuel	233	NO biofuel	3.6
NO power plants	21.3	NO ship	10.2

322 gas-phase thermal reactions, and 81 photolytic decompositions that account for both stratospheric halogen chemistry and tropospheric non-CH_4 hydrocarbon chemistry. A tracer has been added that measures the age-of-air (AOA) with respect to the surface, which is useful for diagnosing the strength of the mean meridional circulation in the stratosphere. Photolytic decomposition uses the Fast-JX photolysis scheme, which is an outgrowth of the Fast-J scheme of *Wild et al.* [2000] for tropospheric photolytic reactions and the Fast-J2 scheme of *Bian and Prather* [2002], which treats stratospheric photolytic reactions. Stratospheric heterogeneous chemistry is handled as in StratChem. GMI-STM also accounts for the heterogeneous effects of aerosols on tropospheric chemistry. The aerosol distributions can be specified from external data sets provided by the GMI project, or can be imported as global distributions from GOCART.

GMI-STM's default emission scenarios for volatile organic compounds (VOCs), NO, and CO due to biomass burning and from fossil and biofuels are documented in Tables 1 and 2, respectively. Surface fluxes from other CH_4 sources, including for example oceans, termites and swamps, amount to 540 Tg yr^{-1} [*Patra et al.*, 2011], and are ingested from a static data set of twelve monthly averages. An additional source of CO is biogenic emissions, which are parameterized with the Model of Emissions of Gases and Aerosols from Nature (MEGAN) [*Guenther et al.*, 2000]. MEGAN generates fluxes of isoprene and monoterpenes after importing the leaf area index, two-meter air temperature, and photosynthetic active radiation from GEOS. The temperature effect on leaf emissions is computed as a function of both the current temperature and the average 2-meter air temperature over the previous 15 days [*Guenther et al.*, 1999]. Biogenic production of CO is then assumed to be from methanol oxidation, whose flux is scaled from isoprene. In a similar manner, production of CO from monoterpenes is scaled with a constant that assumes instantaneous oxidation even though the lifetime of intermediate species is on the order of hours or days. The scaling is necessary because biogenic sources are not resolved at horizontal resolutions currently used in global chemistry models. In tests conducted with earlier versions of GEOS, isoprene production was 635 Tg yr^{-1}, which compares favorably to *Guenther et al.* [2006], who estimate a range of 500 to 750 Tg yr^{-1}.

A significant additional nitrogen source is lightning. In GEOS, the column flash rate is coupled directly to the simulated convection, as the parameterization is based on an empirical relationship between the flash rate and five predictors: the positive surface temperature deviation from 283K, convective cloud-top pressure, convective available potential energy, convective mass flux, and in-cloud depth of the 263K isotherm [*Allen et al.*, 2010]. Lightning-produced reactive nitrogen is added to the NO concentration, and production is specified a priori to generate approximately 5 Tg nitrogen yr^{-1} [*Martini et al.*, 2011]. It is distributed in the vertical between cloud base and cloud top with prescribed profiles that are dependent on type of convection, shallow or deep, and, for the latter, location, marine or continental. Peak nitrogen production lies near 400 hPa in the tropics. GEOS was used for the sensitivity study of *Liaskos et al.* [2015]. They demonstrate that column NO_x in the model is low-biased compared to observations when the above production rate is assumed, and examine changes to tropospheric O_3 when they enhance the mass of NO_x produced by each flash.

To account for nitrogen emitted by soil microbes, GMI-STM employs the parameterization developed by *Yienger and Levy* [1995]. NO fluxes are computed as a function of vegetation type [*Olson*, 1992], temperature, precipitation history, and fertilizer applications. A fraction of the soil-emitted NO_x is deposited within the tree canopy as a consequence of the oxidation of NO to NO_2, followed by uptake of NO_2 by vegetation [*Jacob and Bakwin*, 1991]. A review of published estimates of global soil NO_x emissions is given by *Vinken et al.* [2014], whose estimate of global above-canopy emissions is approximately 12.9±3.9 Tg yr^{-1}. GMI-STM's canopy emissions are 15 Tg yr^{-1}, which are modestly high-biased with respect to the above and to *Hudman et al.* [2012], and near the top of the range of the models that are quoted.

Section 4 contains several examples of applications of GMI-STM. The first looks at results from simulations of stratospheric O_3 loss in the 20th century and recovery throughout the remainder of the 21st century. The second compares modeled tropospheric column O_3 to recent satellite observations. The third and fourth examples demonstrate how horizontal resolution affects results: Better resolved dynamics improves O_3 concentrations at the ground in a stratospheric intrusion, and high resolution combined with similarly resolved emissions is necessary to drive observed nighttime titration of O_3 in high NO_x environments.

2.3.4 Parameterized CO, CH_4, and OH

A recently added chemistry component encapsulates the scheme of *Elshorbany et al.* [2016], who describe a computationally efficient module to simulate the atmospheric chemistry of the CH_4-CO-OH cycle. Called ECCOH (pronounced "echo"), it is used to generate ensembles of sensitivity simulations spanning multiple decades. Such lengthy experiments are necessary for capturing the nonlinear feedbacks in the cycle, and for understanding CH_4 perturbations and their impacts on climate. ECCOH separates the influence of various causal factors on OH, including overhead O_3 column, NO_x, VOCs, and H_2O, and to subsequently determine how each affects CH_4 and CO. ECCOH gives us the capability to address, for example, the wide variance of simulated OH among various models [*Shindell et al.*, 2006; *Fiore et al.*, 2009; *Naik et al.*, 2013; *Voulgarakis et al.*, 2013].

ECCOH parameterizes the chemistry of tropospheric OH and CH_4 and CO. CH_4 surface fluxes include annually repeating wetland emissions, biomass burning, and anthropogenic emissions [*Patra et al.*, 2011]. Anthropogenic and biomass burning CO emissions are from *Strode et al.* [2015]. Stratospheric concentrations are prescribed [*Elshorbany et al.*, 2016], and CH_4 oxidation is based on reactions with OH, atomic chlorine (Cl), and the first excited state of oxygen, O^1D. The parameterization of tropospheric OH is based on *Spivakovsky et al.* [1990a,b] and *Prather and Spivakovsky* [1990]. Using a set of high-order polynomials that describe the functional relationship between OH concentrations, meteorological variables (pressure, temperature, cloud albedo, and humidity), solar irradiance (surface albedo, declination angle, and latitude), and the chemical fields, ECCOH repro-

duces OH predicted by a detailed NO_x-HO_x-VOC-aerosol photochemical mechanism with an accuracy of 8% in areas with the highest OH abundances (e.g., subtropics and tropics). [*Duncan et al.*, 2000]. Before its use in GEOS simulations of the CH_4-CO-OH cycle itself [*Elshorbany et al.*, 2016], the parameterization was validated in studies of the nonlinear feedbacks of CO and OH [*Duncan et al.*, 2007; *Duncan and Logan*, 2008].

2.3.5 Passive Tracers

The above chemical components produce distributions of trace-gases that can be directed to interact with the other physics components, which in turn, influence GEOS's dynamics. With the passive tracer (TR) component, modelers can instantiate a selection of realistic or idealized tracers that are transported by dynamics, convection, and diffusion, but do not otherwise influence the AGCM's dynamics or physics. Such tracers are useful for studying various aspects of horizontal and vertical transport, including the development and maintenance of inter-hemispheric gradients, the location and permeability of the tropopause, and origin of air masses [*Orbe et al.*, 2015]. TR is designed to be flexible and extensible within each class of tracers so that the tracer instantiations can be configured completely by a set of resource files. This philosophy promotes run-time decision-making and reusability of the executable when instantiations are added or removed from the existing tracer classes.

Table 3 lists some examples of the tracer classes currently implemented. Across the classes, sources and sinks can be obtained by reading external files, by linking with GCM fields, or by using radioactive decay rates of other tracers. Methods for depleting the tracers include using fixed loss rates and rates that vary in both time and space to mirror those of chemically active constituents, and specifying *e*-folding and half-life periods. Tracers can also be subject to wet and dry deposition. Source and sink regions can be configured with masks or enabled in domains bounded by longitude, latitude, and height. For example, the constant-burden tracer is emitted only at the surface and is constrained to maintain a constant global mass in the presence of a 90 day *e*-folding loss rate. The AOA tracer is incremented by the time step length each iteration, except in the surface layer where it is reset to zero. Inventories of anthropogenic CO surface emissions constitute the source fluxes of the surrogate CO tracer, and methyl iodide (CH_3I) is instantiated with a constant oceanic emission. Each has a configurable *e*-folding loss rate. Finally, the stratospheric source tracer is emitted only at pressures less than 80 hPa. The diagnostic capabilities of TR's tracers are detailed in the references that accompany Table 3.

Tracers, whether passively advected or chemically active, that are tied to emissions from selected sources are called "tagged tracers," or "tags." Since tags can be multiply instantiated, plumes can be isolated to and followed from certain activities, for example, biomass burning versus combustion of fossil fuels in power plants. Tags can also be configured to capture in-kind emissions on local, regional, or global scales, which enables geographic attribution downstream. A number of tagged tracers are issued as products from the GEOS DAS forward processing system and are available in the MERRA-2 reanalysis. An example is given in Section 4.4, in which CO loss is parameterized by providing a global OH field and a temperature-dependent kinetic rate constant. Forecasts of tagged tracers have been instrumental in the GMAO's support of NASA-sponsored air sampling missions, where they are used by the on-site science teams to aid flight planning.

2.4 Computing Expenses

Increases in resource utilization that accompany the use of the GMAO's more comprehensive chemical mechanisms are compounded by their application to finer scales. Figure 1 illustrates computing costs, defined as the number of processors allocated to a job multiplied by its wall clock time, in a set of ten-day GEOS experiments with the three indicated mechanisms. The simulations are performed on the cubed sphere at each of five resolutions from c48 to c720, which approximates 2° to 1/8°. If instead the abscissa is the logarithm of

Table 3. Some examples of optional passive tracers.

Tracer description	Purpose	Reference
Age-of-air (AOA)	Generate mean age and age spectra. Constrain diffusive processes.	*Waugh and Hall* [2002]
Constant global mean mixing ratio, 90 day lifetime	Differentiate stratospheric and tropospheric air. Find distance from the tropopause.	*Prather et al.* [2011]
Radon-222	Test convective transport, PBL depths, and continental influence on marine air.	*Jacob and Prather* [1990]
Methyl iodide	Diagnose outflows from marine convection and constrain vertical mixing rates.	*Bell et al.* [2002]
Lead-210	Interpret variations in aerosols due to moist processes.	*Considine et al.* [2005]
Stratosphere source, 25 day lifetime	Determine depth of stratospheric intrusions and volume of stratosphere-troposphere exchange (STE).	*Eyring et al.* [2013]
Surrogate CO, 50 day lifetime	Study the impact of circulation changes on pollutant concentrations and transport of emissions.	*Shindell et al.* [2008]
Sulfur hexafluoride	Derive transport time scales and identify barriers to large-scale mixing and transport.	*Manzini and Feichter* [1999]
Beryllium radionuclides	Diagnose meridional transport in the stratosphere and STE.	*Jordan et al.* [2003]

the number of cells, the slopes of the three lines (not shown) connecting the processor hours used for PCHEM, StratChem, and GMI-STM are 1.077, 1.037, and 1.042, respectively, and the lines are reasonably straight and parallel. Hence, processor hours consumed at c48 can be used to predict the costs of higher resolutions for each of the three mechanisms as long as there are no other changes to the configurations.

The source of cost increases varies depending on the changes made to the configuration. For example, profiling c360 PCHEM and StratChem experiments that use 840 processors shows that the latter chemistry component costs 132% more in this configuration, and since the number of transported species jumps from 7 to 51, the cost for horizontal advection increases by 42%. But, in fact, advection accounts for 59% of the combined cost increase. On the other hand, when transitioning c360, 1680-processor experiments from StratChem to GMI-STM, the increases are 623% for chemistry and 4% for advection. In this case, advection accounts for only 2% of the combined change, even though GMI-STM has 20 more transported constituents.

Other performance tests show that run times from PCHEM experiments conducted at c180 (not shown) fall by a factor of only 2.2 when the number of processors is quadrupled (216 to 864). This is because components that require interprocessor communication, such as dynamics and transport, and those that lack load balancing, such as the land-surface, do not scale well. The chemistry components avoid the former because they do not need information from their neighbors on the same layer. So scalability is limited if the time to reach a solution averaged over the cells on each processor is globally non-uniform. We expect spatial inhomogeneities of the chemistry to limit the efficacy of simply adding processors, most notably with StratChem and GMI-STM. However, the fact that entire columns are processed (because there is no vertical decomposition) preserves the averaging aspect. *Long et al.* [2015] show that in GEOS the scaling efficiency of complex (tropospheric) chemistry exceeds that of dynamics as the decomposition approaches the maximum possible for a given resolution.

In practice, project objectives combined with resource availability and turnover dictate which resolutions and chemistry components are chosen. For example, PCHEM is used in the DAS, which operates at c720, because it provides an inexpensive, acceptable first guess for stratospheric O_3 (see Section 4.3). In contrast, GEOS chemistry-climate simulations with GMI-STM (see Section 4.1) have advanced to 1° but rarely beyond, in part because many of the numerous sequential integrations must wait longer for additional processors to become available.

3 GEOS Infrastructure

GEOS architecture uses the Earth System Modeling Framework (ESMF) [*Hill et al.*, 2004] as the core of its infrastructure. Basic ESMF building blocks are gridded components (GCs), and in GEOS a fine-grained approach to component design is employed. For ease of use, a middleware (usability) layer that specifies conventions and best practices for utilizing ESMF in integrated ESMs was developed in GMAO. Funded by NASA's Modeling Analysis and Prediction (MAP) program the layer is termed the MAP Layer, or MAPL [*Suarez et al.*, 2007] (pronounced "maple"). MAPL's primary objective is to reduce the labor of constructing ESMF applications without sacrificing ESMF's generality and extensibility. By encapsulating "boilerplate" functions, it aids in coding a GC's "initialize", "run", and "finalize" methods, provides tools for describing the contents of the "import", "export", and "internal" states (data structures), the latter a MAPL extension of the ESMF_State concept. MAPL also facilitates the use of the ESMF infrastructure layer, and simplifies coupling GCs into complex applications, such as GEOS.

MAPL adopts a hierarchical approach to its architecture, and uses both composite GCs and ESMF coupler components to establish connections between members of the hierarchy.

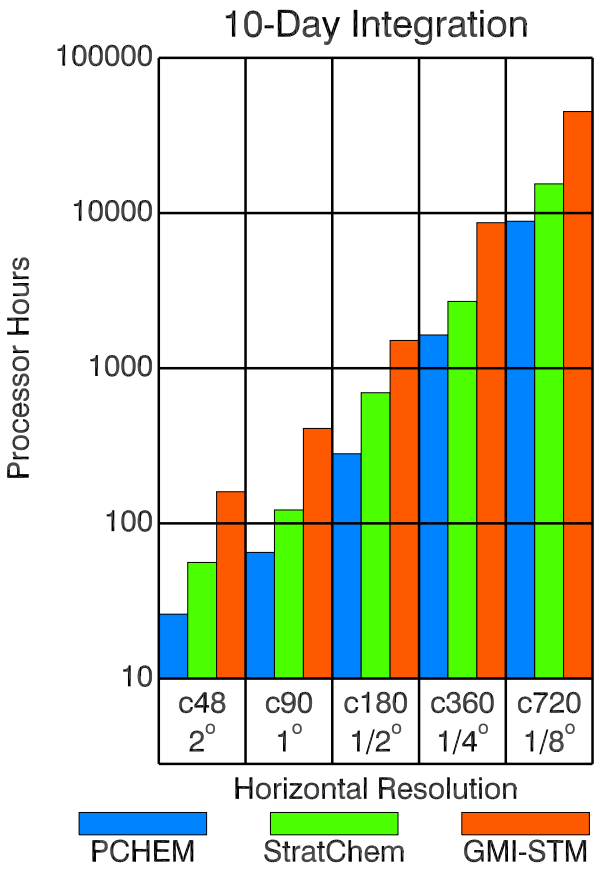

Figure 1. Resource utilization during 10-day GEOS integrations configured to use PCHEM, StratChem, or GMI-STM at five resolutions on the cubed sphere: c48, c90, c180, c360, and c720. Approximate cell size is labeled on the horizontal axis. Processor hours are given on a logarithmic scale.

The relationships among the different members of the hierarchy are articulated using an analogy to familial relationships. MAPL adopts ground rules for the behavior of GCs and provides a standard recipe for writing them. For example, MAPL contains generic versions of the different GC "methods" which, among other functions, create, allocate, initialize, and destroy state items, read and write the elements of the internal and import states, and establish connectivities among other GCs. This approach dramatically reduces the volume of written code while preserving the ESMF flavor of the software. GEOS architecture requires that its components display a MAPL interface.

3.1 Hierarchy

Figure 2 illustrates the hierarchical structure of GEOS as it is configured for the experiments discussed in Section 4, with each box in the figure representing a GC. The black lines in the diagram connect "children" to their "parent" composite GCs. At the top of GEOS's hierarchy is the CAP, which is the main program. It contains the time loop that calls the hierarchy of run methods. After all of them have completed, CAP advances the clock and calls HISTORY, the GC that creates and populates output datasets. Upon expiration of the time loop, CAP runs the finalize methods and writes checkpoint files. It also updates the CAP restart file with the date and time of day, which is available to establish the starting time of the next sequential integration in the experiment, whose temporal length is also declared in the CAP resource file.

Further down the hierarchy, for example, are the two children of DYNAMICS, FV and FV cubed, which host the finite-volume advection core for regular latitude-longitude and cubed sphere grids, respectively. All the results shown in Section 4 are generated on the latter, and, in fact, the former is now rarely used. ATMOSPHERE and OCEAN are two children of GCM. For this paper, all GEOS chemistry experiments are produced with sea surface temperatures and sea ice content prescribed from either observations or data sets archived by atmosphere-ocean GCMs. In this diagram these are the "Data Ocean" and "Data Sea Ice" children of OCEAN. Version 5 of the Modular Ocean Model (MOM-5) [*Griffies et al.*, 2005] implemented in GEOS is another child of OCEAN, and is available as an option for coupled chemistry model simulations. For completeness, the incremental analysis update (IAU) GC's is shown as a child of the GCM, but is not discussed. The chemistry GC, which is the focus of the next section, is a child of PHYSICS, whose family is illustrated in Figure 3.

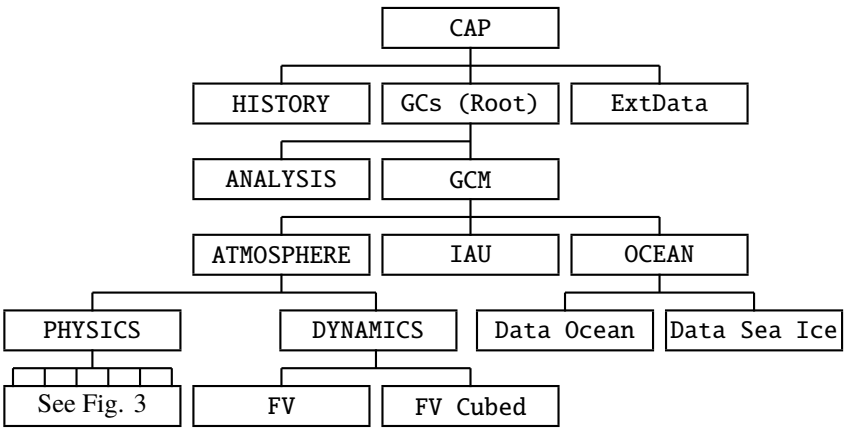

Figure 2. Top-level GEOS hierarchy with black lines connecting child GCs to their parents. Figure 3 examines the children of `PHYSICS`.

In the following sections the reader will find references to the HISTORY and ExtData GCs. Each has been developed to simplify the manner in which experimenters interface with GEOS. Both are critical design elements of GEOS's functionality, and help users to quickly instantiate and run experiments at various resolutions. A description of the capabilities of HISTORY and ExtData may be found in the Appendix.

3.2 Coupling the Chemistry

GEOS's chemistry composite GC appears in the hierarchy as a child of the physics composite GC. At the physics level, the software is directed to connect selected export states of various children to import states of other siblings. Figure 3 illustrates which children of physics supply imports to the GMI-STM, and which of GMI-STM's exports are available to the physics family. In addition, the transported species are made available to dynamics (horizontal and large-scale vertical advection), moist processes (convection), and turbulence (boundary layer mixing) by packing them into an ESMF "bundle," which greatly eases communication. The chemistry "SetServices" method assures that all the species, both transported and non-transported, are included as members of its export state so they are visible to MAPL's history component. For simplicity, other chemistry children, aerosol GCs other than GOCART, and children of radiation are not shown in the figure.

Figure 3 also illustrates GOCART's relationship to GMI-STM. GOCART generates time-dependent global distributions of dust (DU), sea-salt (SS), sulfate (SU or SO_4), and organic and black carbon (OC and BC) aerosols. At run time, the experimenter can toggle any of five switches in the GMI-STM configuration file, one dedicated to each aerosol class, that will establish or break their connectivity. This enables GOCART's predicted aerosols to be imported by GMI-STM and participate in its photolysis computations. Similarly, three of GMI-STM's oxidants, OH, nitrate (NO_3), and hydrogen peroxide (H_2O_2), are available for import to the SU component of GOCART. If the connectivities are not active, MAPL will look to ExtData to fill the imports with fields from external data sets.

As with species concentrations from GMI-STM, the dust and aerosols concentrations from GOCART are bundled for export along with derived aerosol properties, and are imported by the radiative transfer components and by MAPL history, but the connections are not illustrated in Figure 2. To include the effect of scattering due to aerosols, the optical thicknesses are scaled by the single-scattering albedo and an asymmetry factor.

With the configuration of Figure 3, GMI-STM is termed the "radiatively-active-trace-species (RATS) provider" and GOCART is the "aerosol (AERO) provider." PCHEM and StratChem also function as RATS providers. GMI-STM or the new "GOCART.data" GC can function as AERO providers, both in which aerosol distributions are imported from external files via ExtData in lieu of simulation. The choices of RATS and AERO providers and, when applicable, of the chemistry child that provides O_3 to the DAS, are run-time decisions, enforced through the top-level configuration file. That is, the MAPL architecture promotes interchangeability and extensibility. GEOS developers are currently integrating alternative AERO providers, including the Modal Aerosol Model [*Liu et al.*, 2016], and the column-independent version of GEOS-Chem [*Long et al.*, 2015]. The latter provides a more complete tropospheric chemistry mechanism and contains updates to the biogenic and soil emission modules. Further discussion of projected developments can be found in Section 5.

4 Applications

This section describes four applications of the chemical components of GEOS. The object is to highlight the broad range of topics that can be addressed with GEOS chemistry simulations, rather than to offer an in-depth analysis. Where appropriate, references are provided for more detail. For perspective, Table 4 lists a number of the GMAO's projects that utilize GEOS, which is designed to function seamlessly across many different resolutions

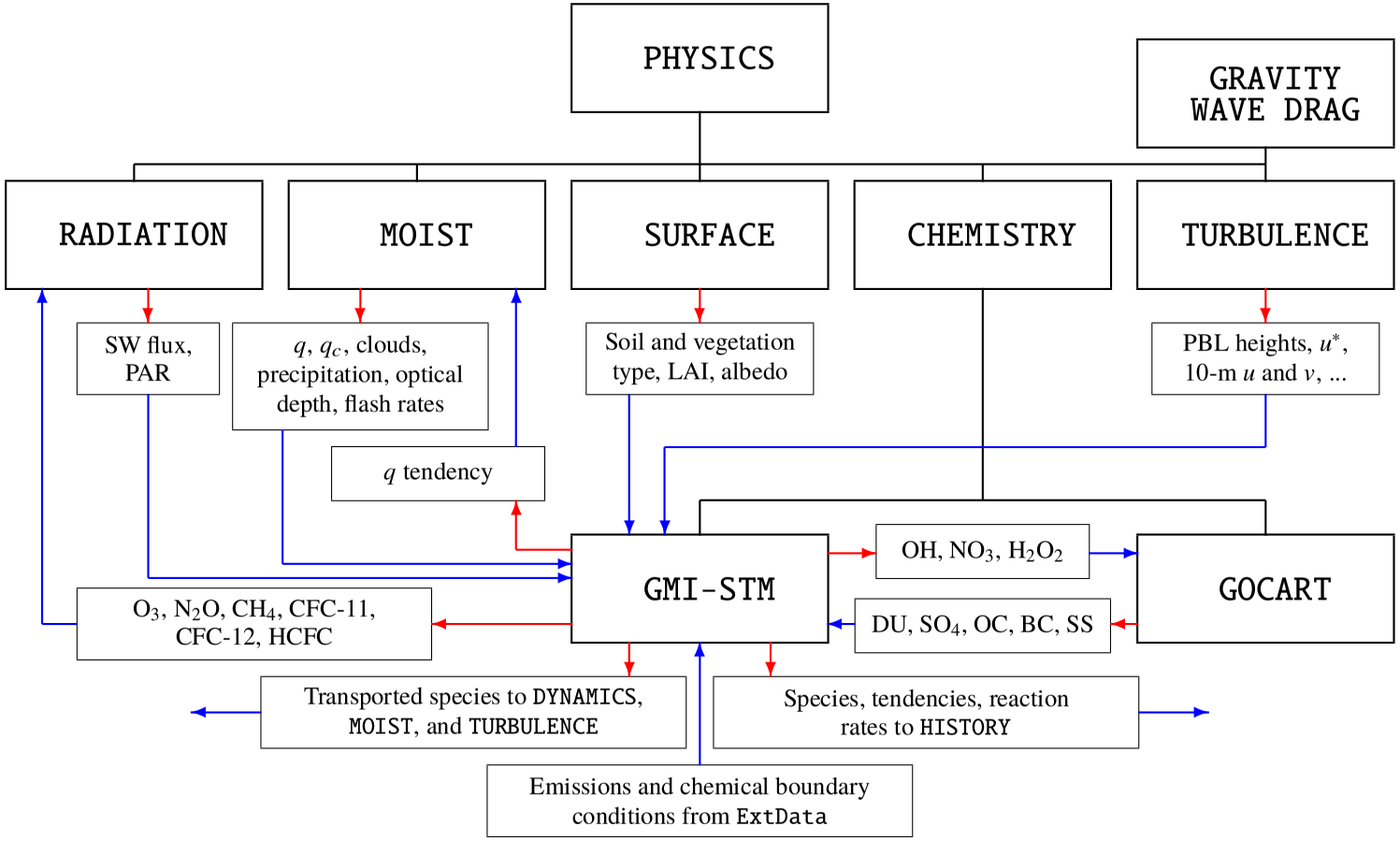

Figure 3. GMI-STM's relationship to the other children of PHYSICS. GCs and their children are connected by black lines. Red vectors indicate exports and blue vectors imports.

Table 4. GMAO activities supported by GEOS

Application	Horizontal resolution range
Global mesoscale simulations	7 km to 1.5 km
Real-time analyses and forecasts	1/8°
Long-term reanalyses	1/2°
Coupled atmosphere-ocean simulations	2° to 1/2°
Coupled chemistry simulations	1° to 7 km
Off-line chemistry and transport (CTM)	1° to 7 km

and applications. While coupled chemistry is the subject of this paper, a closely related application is the GEOS Chemistry Transport Model (GEOS-CTM) which uses the advection, chemistry, and physics components of GEOS (plus ESMF and MAPL) to perform uncoupled experiments. The shared code base between the coupled and uncoupled model configurations means that a model user can run parallel online and off-line simulations, which are useful for understanding and analyzing the impact of chemistry-atmosphere feedbacks.

The discussion of applications is as follows: Section 4.1 examines O_3 depletion and recovery with GEOS configured in a chemistry-climate mode, and compares tropospheric column O_3 to recent satellite observations; Section 4.2 contains two perspectives on coarse- versus fine-scale simulation. The first demonstrates how better-resolved dynamics and topography influence O_3 mixing ratios during a stratospheric intrusion, and the second shows how fine scales affect the simulated chemistry in polluted environments; Section 4.3 illustrates the value of that StratChem brings to forecasts of the size of the Antarctic O_3 hole; and Section 4.4 demonstrates the utility of employing tagged tracers to track plumes of emissions transported by large-scale dynamics.

4.1 Chemistry-Climate

Global AGCMs with coupled chemistry mechanisms, in which the chemical state is influenced by the state of the simulated atmosphere and vice-versa, are called Chemistry-Climate Models (CCMs). CCMs are today's most important tools for understanding the role that atmospheric composition plays in climate change. In GEOS, most CCM applications to date have been run with StratChem or with GMI-STM in tandem with GOCART (as illustrated in Figure 3). The latter configuration is used for our most recent participation in the Chemistry-Climate Model Initiative (CCMI, `http://www.igacproject.org/CCMI`), in which boundary conditions and reference trace gas forcing scenarios were specified by the CCMI Scientific Steering Committee. The supporting experiments span the latter half of the 20th and all of the 21st centuries, which enables simulation of O_3 depletion during the 1980s and early 1990s due to the increase in halogens, and the expected O_3 recovery over the next several decades as halogen loading declines. The surface concentrations of ODSs and GHGs in this GEOS CCM simulation are from the A1 2014 scenario of *Velders and Daniel* [2014] and RCP 6.0 [*Meinshausen et al.*, 2011; *Moss et al.*, 2010], respectively.

Figure 4 shows the simulated annually averaged quasi-global (60°S-60°N) total column ozone ($QGTCO_3$) from 1960 to 2100 from a (REF-C2) CCMI experiment configured as above, with GOCART aerosols coupled to GMI-STM. Also plotted are ground-based [*Fioletov et al.*, 2008] and satellite-based measurements from NASA's Total and Profile Merged Ozone Data Set version 8.6 [*Bhartia et al.*, 2013; *Frith et al.*, 2011]. GMI-STM captures the halogen-induced O_3 decline through the middle 1990s, though the interannual variations

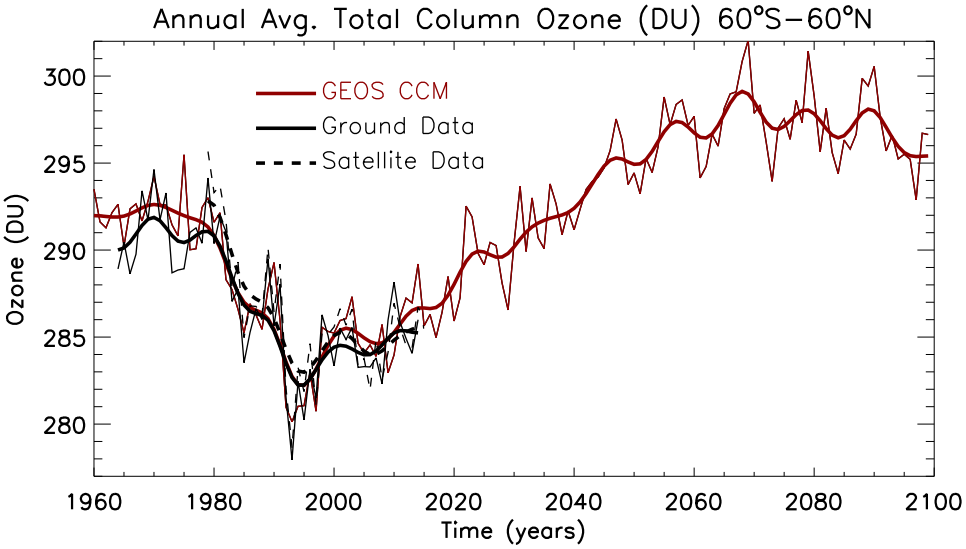

Figure 4. Quasi-global (60°S-60°N) annual average (thin curves) and low pass filtered (thick curves) total column O_3 (Dobson units, DU) from three datasets: (red) GEOS CCM from 1960-2100, (solid black) ground-based observations from 1964 through 2014, and (dashed black) satellite-based measurements from 1979 through 2015.

differ from observations because the dynamics in this experiment are not constrained. This version of the GMI-STM includes solar cycle variability in the Fast-JX photolysis code, and better simulates the sub-decadal O_3 variability compared to observations. The scaling of actinic fluxes uses *Lean* [2000] for 1960 through 2016 and the mean of the most recent four solar cycles for the remainder of the 21st century. A similar solar cycle data set and implementation is described by *Swartz et al.* [2012].

Recovery to O_3 amounts observed in the 1960s occurs by 2040. But because of cooling in the stratosphere attributable to increases in GHGs, the rates (not shown) of several temperature-dependent gas phase reactions that destroy O_3 slow down [*Haigh and Pyle*, 1982]. Hence, the $QGTCO_3$ in the second half of the 21st century is projected by the simulation to be higher than it was in the 1960s [*WMO*, 2010]. Compared to observations of $QGTCO_3$ over the past 50 years, GEOS is among the best performing CCMs [*WMO*, 2014]. The generally decreasing O_3 after 2070 is largely attributable to CH_4, which is projected by the RCP 6.0 scenario to decline.

A (REF-C1) simulation that includes observed sea surface temperature, sea ice concentrations, and trace gas emissions was also performed for CCMI. Figure 5 shows the simulated tropospheric partial column O_3 as a function of latitude and month of year compared to an observational data set derived from the residual of OMI and MLS observations [*Ziemke et al.*, 2011]. Since the simulation ends in 2010, we compared the six-year data overlap period of 2005 through 2010 with observational estimates and found that differences are typically less than a few Dobson units (DU). The causes of the 4 to 6 DU bias in the Northern Hemisphere subtropics and middle latitudes in autumn and winter seen in the bottom panel are under investigation. Uncertainties in the OMI/MLS dataset are not much smaller than the bias. The larger negative biases in the Southern Hemisphere high latitudes are due to an issue with the satellite-derived residuals. In this region, the simulation agrees much better with the ozonesonde-based climatology of *McPeters et al.* [2007] as illustrated in Figure 4 of *Ziemke et al.* [2011].

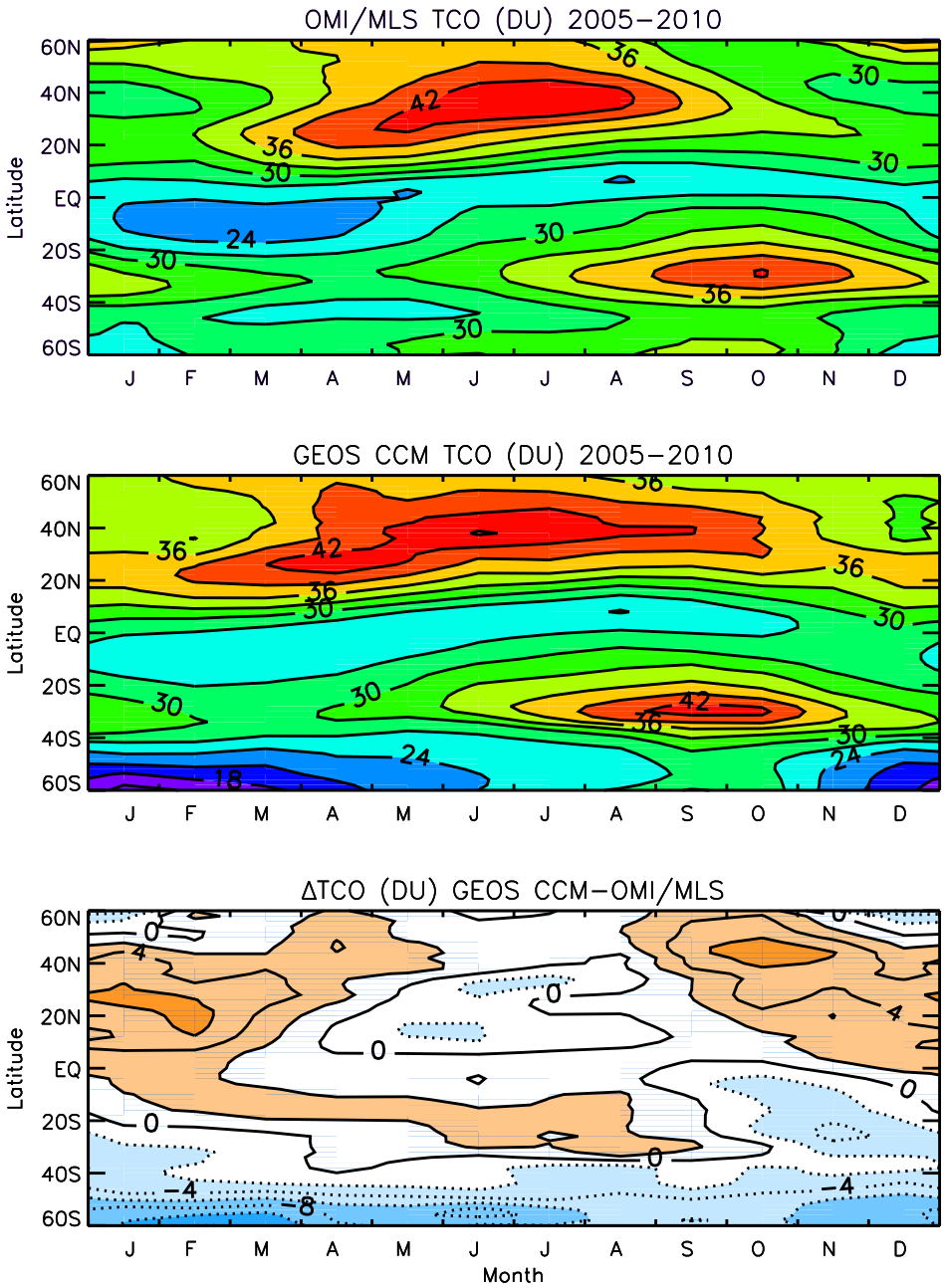

Figure 5. Six-year averages of tropospheric partial column ozone (DU) from (top) the OMI/MLS residual [*Ziemke et al.*, 2011], (middle) the REF-C1 GEOS CCM simulation, and (bottom) their difference.

4.2 Flexible Horizontal Resolution

GEOS allows model users to select a wide range of horizontal resolutions applied globally, including (approximately for the cubed sphere) 2°, 1°, 1/2°, 1/4°, 1/8°, and 7 and 3.5 km. This enables configuration and execution of sets of simulations that utilize a common executable and the same boundary conditions to assess the influence of resolution on transport and chemistry.

For an example of the impact on transport, Figure 6 illustrates GEOS's surface-layer O_3 concentrations during each of four MERRA-2 meteorology "replay" simulations of a stratospheric intrusion over the western United States on Friday 6 April 2012. Replay is similar to the incremental analysis update method [*Bloom et al.*, 1996] used in the GEOS DAS to apply the analysis as a correction to the background. However it uses pre-existing analyses to produce the increments. Observed (United States Environmental Protection Agency Clean Air Status and Trends Network) mixing ratios rose to 79 parts per billion by volume (ppbv) in Denver, CO, 84 ppbv in Rocky Mountain National Park, and 76 ppbv at Centennial, WY. As GEOS is configured sequentially toward higher horizontal resolution, it progressively captures more spatial detail in the intrusion's footprint, and it generates concentration maxima that are closer to the surface observations. MERRA-2 analyses are archived at 1/2° horizontal resolution.

Diagnosis of the O_3 budget (not shown) reveals that O_3 tendencies in the intrusion are overwhelmingly dominated by transport, especially at high resolution, suggesting that finer discretization improves the representation of jet stream dynamics and downward vertical motion in the intrusion (See Fig. 6 in *Newton and Trevisan* [1984]). Also important is the representation of mountain topography. Peak elevations are more realistic at high resolutions, which makes it more likely that descending O_3 will impact the surface in mountainous regions. GMI-STM is used in these experiments. *Ott et al.* [2016] provide more details about stratospheric intrusions simulated by GEOS, and discuss the implications for tropospheric O_3 budgets.

To demonstrate another aspect of resolution dependence, we focus on the nonlinear behavior of chemical reactions by examining how surface NO_x and O_3 concentrations evolve during parallel 1/8° and 2° analysis-driven replay simulations of eight days length in early May 2011. Both experiments use a copy of the inventory of surface anthropogenic emissions. During each of the eight days, we determine the maximum NO_x concentration that is attained in each surface cell in the 1/8° simulation. At the end of each day (UTC), we extract the locations of the cells with the fifteen highest concentrations, with the condition that none are within 2° of each other. The time series of both NO_x and O_3 concentrations in each of the fifteen selected cells is then collected from noon before (local time) to noon after the peak NO_x concentration occurred. The sampling yields 120 unique diurnal cycles for each trace gas. A second set of diurnal cycles is obtained from the 2° simulation, wherein each day's chosen cells are collocated with the fifteen from the same day of the 1/8° run.

The average diurnal cycles of NO_x and O_3 from each of the two sample groups are depicted by the blue and orange curves in Figure 7. In both simulations, NO_x concentrations increase after sunset, which contributes to the overnight decline of O_3. But because the selected 1/8° cells are most often located near strong emitters, and the mass from each is distributed throughout a volume that is approximately 0.4% that of the collocated 2° cell, NO_x concentrations on average grow by sunrise to more than an order of magnitude greater than in the 2° simulation. Even though middle-afternoon O_3 concentrations are about the same in both simulations, between 45 and 50 ppbv, the elevated localized NO_x drives nighttime O_3 to near zero [*Brown et al.*, 2012] at 1/8°, whereas at 2° the average falls no lower than 28 ppbv. A third sample is collected from the 1/8° simulation: the surface concentrations averaged over the 16x16 matrix of cells that are collated with each respective member of the sample from the 2° simulation. Their averaged diurnal cycles drawn in green. Across the day, NO_x concentrations on average consistently exceed those in their 2° counterparts, but

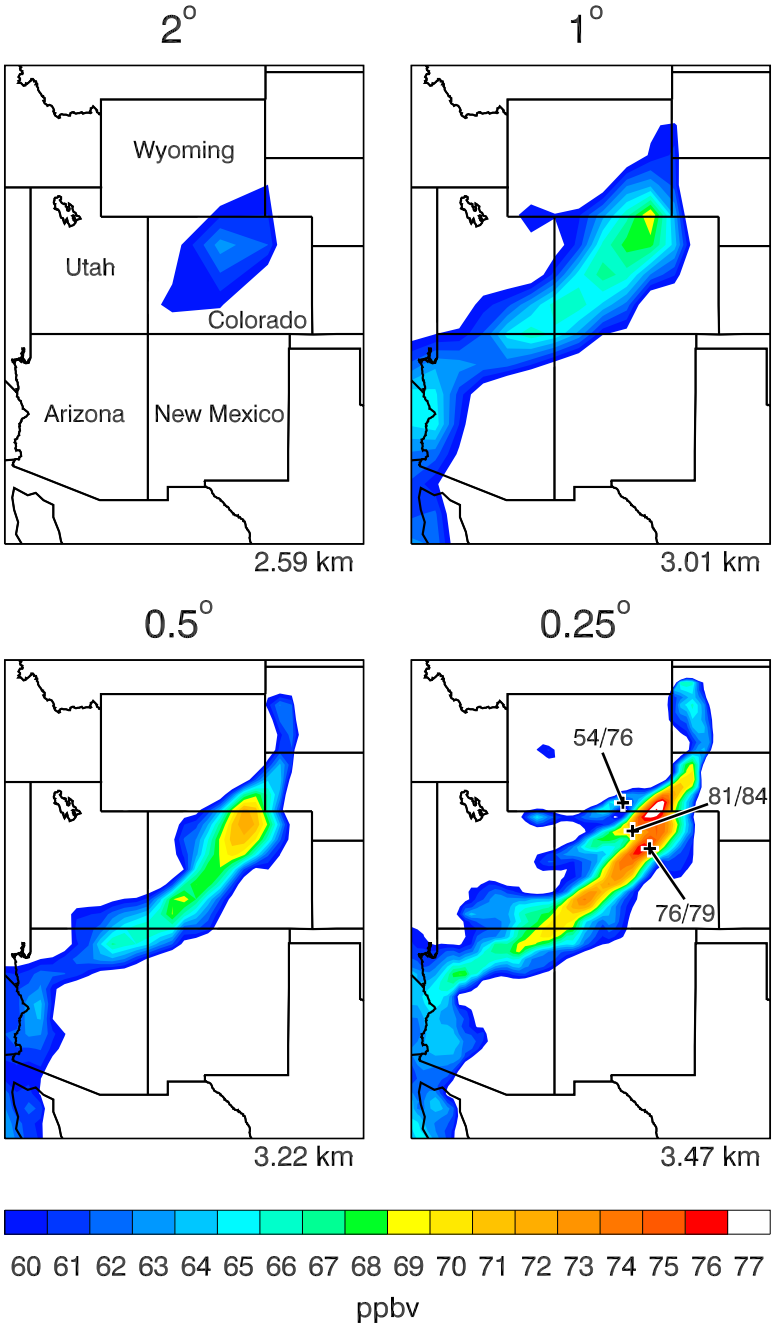

Figure 6. Surface O_3 concentration at 6PM MDT on Friday 6 April 2012 from four simulations of a stratospheric intrusion that are identical except for the labeled horizontal resolution. Observed current/peak-event volume mixing ratios (ppbv) at the three locations mentioned in the text are drawn on the lower-right panel. At bottom-right of each panel, GEOS's highest elevation in Colorado is indicated. 880m is gained when discretization is enhanced by a factor of eight.

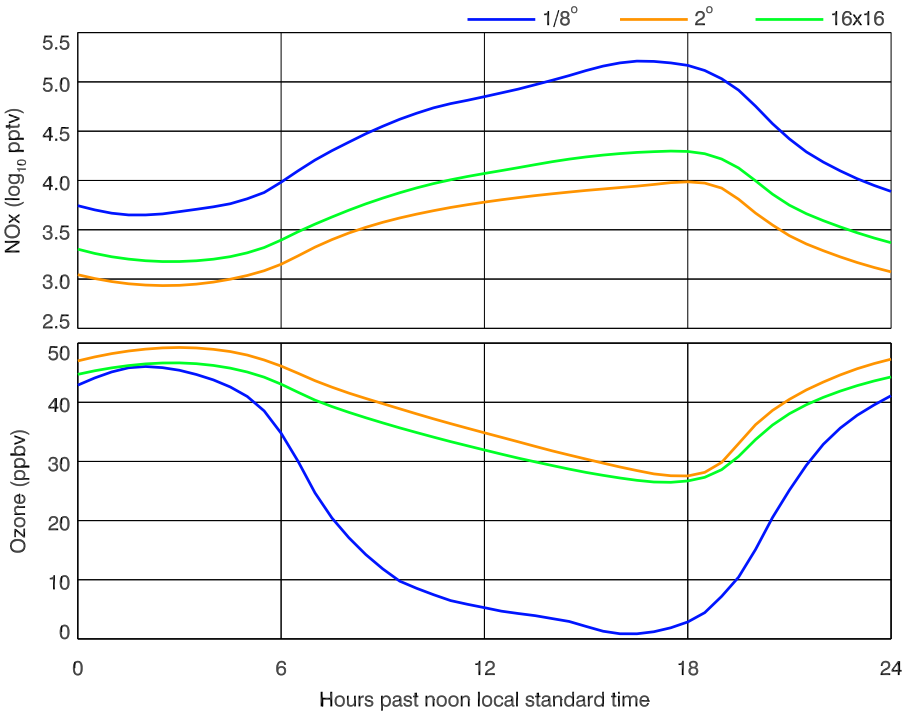

Figure 7. Mean diurnal cycles of NO_x (top) and O_3 (bottom) surface concentrations from the 15 highest-NO_x locations during each of eight May days of companion 1/8° and 2° simulations. The three sample sets are: 1. High-NO_x cells from the 1/8° simulation (blue). 2. The collocated cells from the 2° simulation (orange). 3. The average of the concentrations in the 16x16 matrix of 1/8° cells with the same footprint as each respective 2° cell (green). Note that the NO_x ordinate is scaled logarithmically and O_3 is scaled linearly. The sample size is 120.

the O_3 concentrations do not substantially differ from the 2° values. This example demonstrates that both highly localized emissions and a model discretization that is fine enough to resolve them are required in order simulate NO_x concentrations large enough to promote nighttime O_3 titration that is observed in polluted air.

This result and the intrusion example presented above highlight two aspects of the tropospheric O_3 budget that might be important when considering the cost of horizontal resolution. Historically, the expense of discretization has driven chemical modelers investigating this class of phenomena to operate in limited regions with fine meshes that are interfaced with coarser meshes applied globally or with components that provide boundary conditions. In contrast, GEOS is now capable of simulating mesoscale-dependent chemistry and transport uniformly worldwide with relative efficiency, in part by eliminating the need to engineer the software needed to support embedded meshes and their connecting modules in a general way.

4.3 O_3 Depletion in the Data Assimilation System

For the application described here, simulations are performed with the GEOS three-dimensional variational DAS version 5.13.1, which is based on the Gridpoint Statistical Interpolation (GSI) approach described by *Wu et al.* [2002]. Global analyses are generated using six-hour data windows in which observations are combined with background states produced by the GEOS AGCM. Meteorology is constrained by satellite radiance data and by conventional observations. PCHEM (Section 2.3.1) is the default chemical component in the GEOS DAS because it executes quickly and enables the GMAO to meet production schedules, and because it provides an acceptable background stratospheric O_3. Driven by efforts to assimilate more trace species, including CO and CO_2, and by requirements for generating high-fidelity and high-resolution O_3 fields for observing system simulation experiments (OSSEs), the GMAO is investigating whether improvements that could come from an operational utilization of StratChem (Section 2.3.2) are worth the added computational expense. In the current DAS, there is no covariance structure that relates O_3 to other species or to temperature.

The O_3 assimilation is described by *Wargan et al.* [2015], who demonstrate that the GEOS-5 analysis performs well when compared to ozonesondes in the lower stratosphere where it is strongly constrained by MLS profile data. In addition, *Gelaro et al.* [2017] show that in MERRA-2 the size of Antarctic O_3 holes, defined as the area of the Earth's surface enclosed by the 220-DU contour of total column O_3, agrees well with TOMS and OMI observations from 1980 through 2015.

Figure 8 illustrates results from a 2° GEOS DAS simulation with StratChem that spans September 2015. The time period covers the developing and mature phases of the Antarctic O_3 hole. The size of the hole is indicated by the solid black line, which traces the growth of the area in million square kilometers throughout the month. From the analysis, two sets of ten-day forecasts are launched at 21:00 UTC daily between 1 and 20 September. One set of forecasts is generated with PCHEM and the other with StratChem, and the predictions of the O_3 hole's size are drawn in red and blue, respectively. Since O_3 retrievals from MLS and OMI are assimilated during the DAS, total O_3 from the GEOS DAS serves to validate the forecasts.

PCHEM's forecasts are poor because its loss coefficients, which are tied to monthly means of a two-dimensional model's steady state, contain only a weak signal of the Antarctic O_3 hole. Thus, immediately after initialization PCHEM drives O_3 away from the analysis toward higher mixing ratios in the ozone hole, which raises total O_3 and reduces the ozone hole's area. On the other hand, StratChem shows good forecast skill because it explicitly partitions Cl beteween its active and reservoir species, and generates sufficient concentrations of ClO to drive heterogeneous loss as the sun rises on the pole. In fact, the root-mean-square

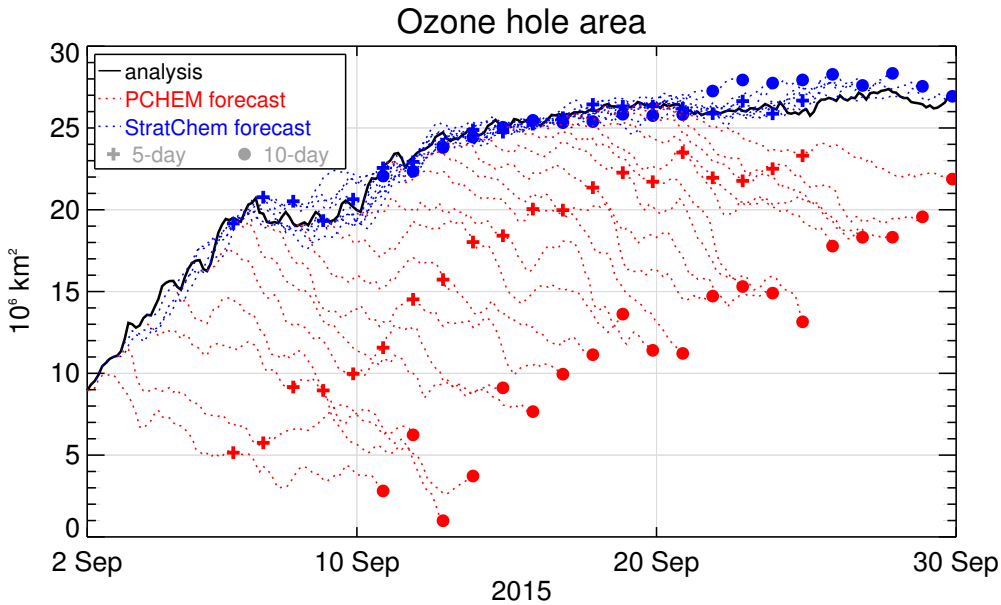

Figure 8. Area of the 2015 Antarctic O_3 hole in the DAS (solid black) and during ten-day forecasts with PCHEM (dashed red) and StratChem (dashed blue). Crosses and circles show the areas in each forecast at five and ten days, respectively.

difference from the analyzed area stays within 4%, and the mean difference is less than 1% at ten days.

Further studies with this configuration of the DAS are being conducted to examine Cl partitioning in two anomalously cold Arctic winters that have long periods of low temperatures and high levels of Cl activation. Early results combined with those above demonstrate that by accepting modest increases in resource utilization, chemical forecasts for the stratosphere can now be a production system reality. In addition, these experiments show that accurate chemistry mechanisms can now be used in the DAS to quantify processes that operate on stratospheric O_3 and generate error estimates.

4.4 Tagged Tracers

As mentioned in Section 3 GEOS's infrastructure permits multiple instantiations of atmospheric tracers, a feature that is most often used in the "tracer gridded component" (TR) and in GOCART. Using surface sources as an example, the model user can define a tracer with characteristics of a realistic trace gas that has emissions in a specified region, or in any assortment of grid cells, by applying a mask. The evolution of a plume attributable to a particular source, or collectively the plumes from a set of sources, can then be followed by monitoring the "tagged tracer" emitted from the cells particular to each mask. That is, each tagged tracer has its own mask and is independently transported. In principle, hundreds of tagged tracers allocated across a spectrum of emissions can be run simultaneously. Notably, each tagged tracer has its own output stream, so we can examine the evolution of either individual plumes or groups of plumes whose members can be chosen at will.

Tagged tracers are valuable for investigating the spread of pollution and the relative contribution of local and remote sources to the degradation of the air quality. Figure 9a is a map of three tagged CO tracers (advected, but not assimilated) taken from the GEOS DAS forward processing system at 18:00 UTC 29 July 2016. The tags are identified by color.

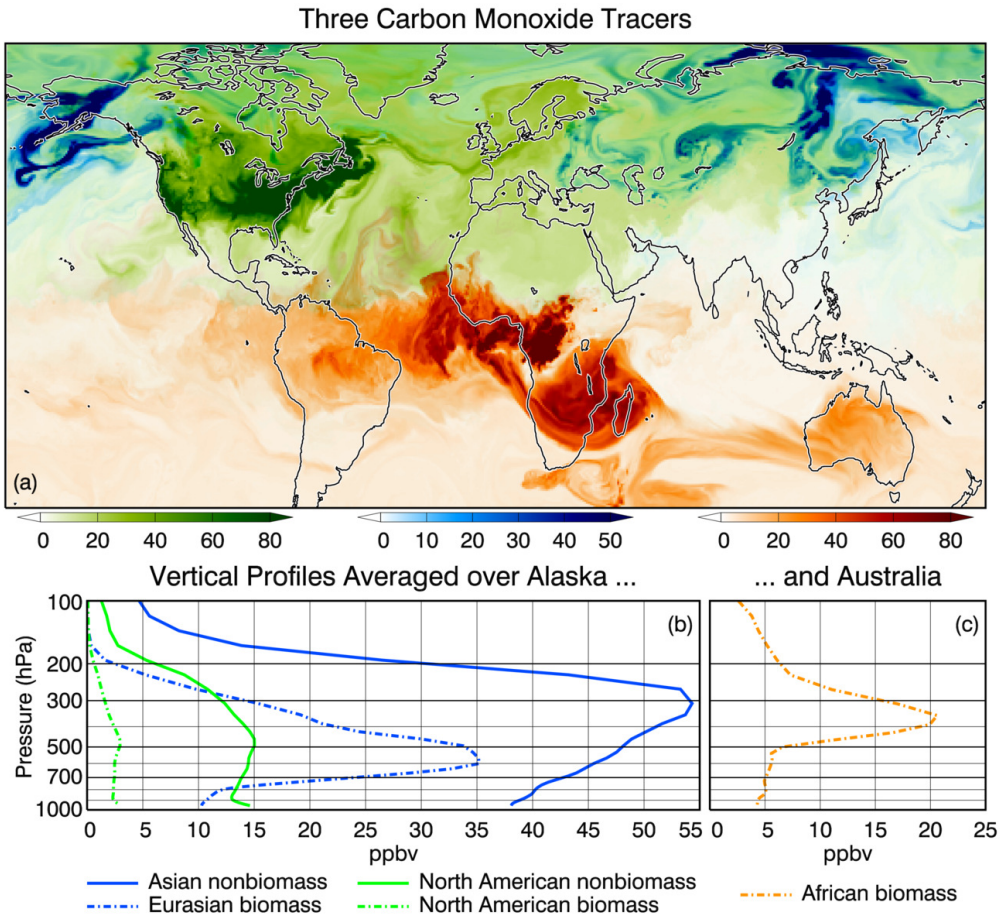

Figure 9. Top: Distribution of three tagged tracers from the GEOS DAS forward processing system. Green: CO from North American non-biomass burning emissions plotted at the surface. Blue: CO from Eurasian biomass burning plotted at 500 hPa. Orange: CO from African biomass burning plotted at 375 hPa. Darkest shades indicate highest concentrations. Bottom: Vertical profiles of CO tagged tracers averaged over (b) Alaska and (c) Australia.

Green shows the surface concentration of CO from biofuel, fossil fuel, and biogenic (non-biomass) emissions over North America, blue is CO plotted at 500 hPa from Eurasian biomass burning, and orange is CO plotted at 375 hPa from African biomass burning. Because the emissions are transported by analyzed winds, the plumes should bear some resemblance to reality and offer a diagnostic tool that can be used in near-real time to identify remote sources as contributors to local pollution both at the ground and throughout the free troposphere. At the instant of the snapshot, a dense plume from Eurasian biomass burning is transiting Alaska. African emissions are bifurcated, with those close to the equator traversing the Atlantic Ocean to South America and those at more southerly latitudes crossing the Indian Ocean to Australia. Surface winds are strong enough to bring North American emissions to Europe, and, in fact, the pollution is present throughout the Arctic [*Shindell et al.*, 2008; *Thomas et al.*, 2013]. In this application, CO loss is parameterized as described in the closing paragraph of Section 2.3.5.

The instantaneous, area-averaged vertical distribution of five CO tags, including the three in the snapshot, are plotted in Figures 9b and 9c. The profiles due to North American and Eurasian emissions are averaged over Alaska, and the profile due to African emissions is averaged over Australia. Concentrations peak in the middle and upper troposphere as a result of the dynamics of long-distance or intercontinental transport [*Stohl et al.*, 2002; *Cooper et al.*, 2004]. By vertically integrating the concentrations of both the tagged tracers and the global CO that contains all emissions and then converting to mass, we can obtain the respective contributions of the tags to the total CO. Asian nonbiomass and Eurasian biomass burning taken together account for 60.4% of the total (column) CO over Alaska. North American emissions together contribute substantially less, 14.5%. Over Australia, 12% of the CO is attributable to biomass burning in Africa.

5 Projected Developments

Several updates to StratChem are undergoing testing and validation, and will be included in model versions to be released in the near future. A major upgrade is the addition or reassignment of 18 transported species that include both short- and long-lived ODSs and GHGs identified by the World Meteorological Organization (WMO) Ozone Assessments as essential to radiative forcing. The first twelve include two CFCs (CFC-114 and -115), two HCFCs (141b and 142b), three Halons (1211, 1202, and 2402), and five very-short-lived (VSL) bromocarbons [bromoform ($CHBr_3$) and dibromomethane (CH_2Br_2), CH_2BrCl, $CHBr_2Cl$, and $CHBrCl_2$]. The latter are required for an accurate representation of the stratosphere's bromine budget and obviate the need to artificially enhance CH_3Br as mentioned in Section 2.3.2. The remaining six gases are hydrofluorocarbons (HFC-23, -32, -125, -134a, -143a, and -152) that have strong global warming potentials. In addition to broadening the mechanism, the experimenter can now choose to reference surface flux scenarios in lieu of mixing-ratio boundary conditions for eight gases: CFC-11, CFC-12, CFC-113, CH_3CCl_3, carbon tetrachloride (CCl_4), HCFC-22, $CHBr_3$ and CH_2Br_2. To maintain realistic tropospheric mixing ratios in the presence of emissions, a parameterized surface loss of CH_3CCl_3 and CCl_4 is applied over both land and ocean. Since inorganic bromine formed from the degradation of VSL bromocarbons exists mainly in soluble forms, a new wet scavenging method based on model-generated precipitation was implemented for HBr, HOBr and $BrONO_2$. The upgrades are expected to improve StratChem's chemistry-climate simulations and promote GEOS's continued participation in model comparison exercises.

In cooperation with the GMAO, *Long et al.* [2015] adapted Harvard University's GEOS-Chem global atmospheric chemistry model into a grid-independent (GI), ESMF-compliant module. This allows GEOS-Chem to run on unstructured grids, and so is not limited by the domain decomposition for the dynamics. It also allows GEOS-Chem to be run in three modes from the same code base: (1) as a stand-alone CTM, (2) as a coupled component of an ESM, and (3) as a CTM within the ESM's infrastructure. The grid-independant module is now encapsulated in a GEOS GC (a child of CHEMISTRY), and experiments have been con-

ducted with Version 10 of GEOS-Chem in which the stratosphere is prescribed. It produces realistic tropospheric ozone based on results from a MERRA-2 replay downscaled to 1/8°. The GMAO is also testing the unified tropospheric-stratospheric chemistry extension (UCX) [*Eastham et al.*, 2014] in GEOS-Chem Version 11. By maintaining common-code repositories with the GEOS-Chem group at Harvard, the GMAO will have access to the continuous improvements provided by the world-wide GEOS-Chem community.

The GI GEOS-Chem provides an opportunity to operate the chemistry on tiled grids that capture the heterogeneity of properties of the Earth's surface not adequately resolved by regular meshes. This will allow solidification of the connections between GEOS-Chem and other GCs that are exercised on catchments grids and other unstructured grids, including ocean and ice, land-surface, and dynamic vegetation models.

6 Summary

GEOS, the ESM developed by the GMAO and the subject of this paper, is NASA Goddard's research-to-operations platform for data assimilation, numerical weather prediction, and parameterization of geophysical processes, including chemistry. This manuscript documents the current state of GEOS for configurable coupled chemistry applications, which represents the culmination of thirteen years of chemistry-component development, validation, and integration into the evolving GCM. The effort is conducted by the GMAO in collaboration with partners in the Atmospheric Chemistry and Dynamics Laboratory and the NASA Center for Climate Simulation at NASA Goddard, and recently with colleagues in the Atmospheric Chemistry Modeling Group at Harvard University. Among our principle objectives are to use retrievals and radiances from NASA's satellites to guide development of the model and measure its performance, to create a research tool that enables investigation of topics in atmospheric chemistry on widely varying spatial and time scales, to provide a platform that encourages global mesoscale simulation and assimilation of trace gases, and to enable the GMAO to participate in sensor development through production of chemical OSSEs.

The ESMF-based infrastructure of GEOS is discussed and elements of the MAPL middleware layer that are useful for designing chemical components and conducting chemical simulations are introduced. MAPL is shown to encapsulate "boilerplate" functionality and moderate the effort needed to integrate new chemistry components and update them. We provide an illustration of how chemistry components are coupled to the AGCM. Our hierarchical approach, with its parent-child relationships, is shown to provide a straightforward and consistent methodology that promotes extensibility and interoperability as components are added and mature while minimizing the overhead required for connectivity and communication.

Several examples of applications, focusing mostly on O_3, highlight the diversity of atmospheric chemistry and transport topics to which GEOS can be applied. We highlight two results from a GMI-STM configuration designed for chemistry-climate simulations with boundary conditions specified by the CCMI project. GEOS reproduces the decline of global O_3 due to halogen loading through the middle 1990s, successfully simulates the beginning of its recovery, and projects its evolution through the remainder of the 21st century. For the present-day atmosphere, the same configuration is used to compare tropospheric partial column O_3 to satellite observations.

With the objective of demonstrating the advantages of fine-scale discretization, we show how simulated O_3 concentrations more closely resemble surface observations in a stratospheric intrusion as resolution increases. We also show that global 1/8° resolution is capable of simulating dramatic nighttime O_3 loss in polluted air because high NO_x concentrations are maintained near strong emitters that are similarly resolved in the GMAO's emission inventories. Both results suggest that it is important to reevaluate global model-based

tropospheric O_3 budgets that are published in the literature since coarser-scale simulations have to date provided the foundation of global chemistry model bench marking.

We show that forecasts of the size of the Antarctic O_3 hole launched from GEOS DAS analyses generate divergent results when either PCHEM or StratChem are used. The ability of the latter to generate reasonably accurate distributions of reservoir and active Cl species proves valuable, justifies the added expense, and demonstrates that detailed prognostications of stratospheric trace species can now be a production reality. Just as important, coupling StratChem to the DAS unlocks the compelling potential to routinely generate trace gas profiles directly comparable to those that are remotely sensed, which opens up new opportunities for model validation and observing system simulation. Finally, in the only example not directly tied to O_3, we demonstrate how CO tagged tracers that are incorporated in the operational GEOS DAS forward processing system can be used in real time to identify remote contributors to local pollution.

The infrastructure of GEOS, including the use of ESMF and MAPL and the FV dynamical core on the cubed sphere, make GEOS highly flexible, extensible, and scalable, which enables it to absorb the daunting processor and data flow requirements that will be demanded by NASA-sponsored Earth Science research during the coming years. To keep pace with shrinking footprints that attend sensor development, global ultra-fine scale assimilation and simulation will soon be "business as usual," and several new trace-gas data types will be ingested. Grid-independent chemistry components will be coupled to highly-resolved land-surface and vegetation models operating on irregular grids. The exchange of gases between the atmosphere and ocean and land ecosystems will then be explicit and prognostic. As GEOS evolves, it will create opportunities to more accurately simulate the interplay between seasonal climate variations, VOCs, O_3, and regional air quality, and will promote the GMAO's continued participation in model comparison studies focused on determining chemistry's role in climate change.

A: Appendix

A.1 HISTORY

GEOS's history GC manages output streams that the experimenter declares at run time via its configuration file, usually named HISTORY.rc. HISTORY sees the pointers to the export states of each component in the GEOS hierarchy, and assembles the experimenter's list of fields from those states into "collections" as GEOS executes. Several collections can be declared, each with specifications of some or all of the following properties or attributes that are coded into the configuration file:

- Fields can be instantaneous or time-averaged, and all fields within a collection use the same time discretization. Time-averaged data by default are stamped with the central time of the averaging interval.
- Collections are given a common name template, usually with calendar date and time included in the template.
- A beginning and ending time may be specified for each collection, and each file in the collection has the same fixed number of time groups.
- Collections can be written to either flat binary files or to Network Common Data Format (NetCDF) self-describing format files, though the former is now rarely used.

In addition to time interpolation, HISTORY can subset fields and can apply GEOS's utilities to regrid the fields both horizontally and vertically. Through vertical interpolation, output fields can be written, for example, on a given set of isobaric surfaces instead of on the native eta-coordinate levels. But, in fact, the routines operate more generally. That is, as long as the desired vertical coordinate is monotonic over the vertical region of interest and is a member of the export state of a GC in the hierarchy, it can be used as the interpolate. In

the stratosphere, potential temperature meets these requirements, which enables the experimenter to generate collections on isentropic surfaces.

The remainder of the configuration file contains the list of fields in the collection. Each line consists of a comma-separated list with the field's name as it appears in the export state of its owner GC, the name of the owner, and an optional alias. If it appears, the alias will replace the export state name when the data set is written. Aliases are useful, for example, when backward compatibility is required for users' applications. Finally, HISTORY allows specification of derived fields that can be readily defined by an arithmetic expression or function that operates on the existing, or primary, exports. The expression is evaluated using the MAPL parser component. Examples include `SQRT(U*U+V*V)`, `NO+NO2*2.00E0`, and `LOG10(HNO3)`. Since the expression is evaluated element by element, the fields must have the same shape or dimensions, and the order of operations is as in Fortran.

A.2 ExtData

ExtData is an internal MAPL GC, instantiated and run automatically by CAP. It is used to fill import states not satisfied by connectivities in the hierarchy. That is, the pointers to fields that exist in a GC's import state are passed up the GEOS hierarchy until they find an established connectivity to another GC that is able to provide data to fill the pointer. If a connectivity is not found, then the search eventually ascends to CAP, which examines the list of fields in the export state of ExtData for a match. ExtData's export state is established by its configuration file provided by the experimenter at run time, in which each field to be exported is paired with a field variable name on a specified NetCDF dataset or dataset template. In essence, ExtData is a provider of last resort for gridded, geospatial data. For the chemistry GCs, it provides a flexible, encapsulated way to import, for example, biomass, biofuel, and fossil fuel emissions.

After ExtData acquires a field, it is spatially interpolated (regridded) to GEOS's native resolution. Using a directive in the RC file, the data can be regridded in a mass-conserving manner, or it will be non-conservatively regridded with bilinear interpolation. When interpolating the horizontal wind fields from their NetCDF grids, the zonal and meridional components are treated not as individual scalars, but rather as vectors that are properly rotated onto the cubed sphere's six faces. For masks, voting-based directional mapping is used to assure that values on GEOS's native grid remain integers.

For temporal interpolation, ExtData's RC file allows the experimenter to supply a refresh template that describes how often to update the field. ExtData then examines the time variable on the NetCDF files (described by a file template) in search of two that bracket the current time on GEOS's clock. The two time stamps need not be on the same file, as ExtData can interpolate between fields from different files. ExtData provides additional flexibility to specify climatological fields, time offsets, and one-time updates (for time invariance), the latter established only during the initialize methods. Like HISTORY, ExtData also supports derived exports whose names follow the logical requirements of the MAPL parser component.

Acknowledgments
GEOS and the GMAO are supported by NASA's Modeling, Analysis, and Prediction Program under the direction of Dr. David Considine. ESMF is sponsored by the Department of Defense, NASA, the National Science Foundation, and the National Oceanic and Atmospheric Administration. Computations were performed at the NASA Center for Climate Simulation. The GEOS-5 source code is available under the NASA Open-Source Agreement at `http://opensource.gsfc.nasa.gov/projects/GEOS-5`. The version 8.6 reprocessed SBUV merged dataset used in Figure 4 is available from the Atmospheric Chemistry and Dynamics Laboratory (ACDL) (`https://acd-ext.gsfc.nasa.gov/Data_services/merged/instruments.html`), the ground-based data can be found at the World Ozone and

Ultraviolet Radiation Data Centre (http://www.woudc.org/archive/Projects-Campaigns/ZonalMeans), and instructions for obtaining CCMI datasets are available from the British Atmospheric Data Centre (http://blogs.reading.ac.uk/ccmi/badc-data-access). MLS and OMI data used in Figure 5 are available from the Goddard Earth Science Data and Information Services Center as described at https://aura.gsfc.nasa.gov/science/data.html, and the tropospheric column ozone data products are provided by the ACDL (https://acd-ext.gsfc.nasa.gov/Data_services/cloud_slice/index.html). The Environmental Protection Agency surface O_3 CASTNET measurements used in Figure 6 are available from https://java.epa.gov/castnet/clearsession.do. The authors thank three reviewers whose comments greatly improved the manuscript.

References

Allen, D., K. Pickering, B. Duncan, and M. Damon (2010), Impact of lightning NO emissions on North American photochemistry as determined using the Global Modeling Initiative (GMI) model, *J. Geophys. Res., 115*, D22301, doi:10.1029/2010JD014062.

Aquila, V., L. Oman, R. Stolarski, A. Douglass, and P. Newman (2013), The response of ozone and nitrogen dioxide to the eruption of Mt. Pinatubo at southern and northern midlatitudes, *J. Atmos. Sci., 70*, 894–900, doi: 10.1175/JAS-D-12-0143.1.

Bacmeister, J. T., M. J. Suarez, and F. R. Robertson (2006), Rain reevaporation, boundary layer convection interactions, and Pacific rainfall patterns in a AGCM, *J. Atmos. Sci., 63*, 3383–3403, doi:10.1175/JAS3791.1.

Bacmeister, J. T., and G. L. Stephens (2011), Spatial statistics of likely convective clouds in CloudSat data, *J. Geophys. Res., 116*, D04104, doi:10.1029/2010JD014444.

Barahona, D., A. Molod, J. Bacmeister, A. Nenes, A. Gettelman, H. Morrison, V. Phillips, and A. Eichmann (2014), Development of two-moment cloud microphysics for liquid and ice within the NASA Goddard Earth Observing System Model (GEOS-5), *Geosci. Model Dev., 7*, 1733–1766, doi:10.5194/gmd-7-1733-2014.

Bell, N., L. Hsu, D. J. Jacob, M. G. Schultz, D. R. Blake, J. H. Butler, D. B. King, J. M. Lobert, and E. Maier-Reimer (2002), Methyl iodide: Atmospheric budget and use as a tracer of marine convection in global models, *J. Geophys. Res., 107*(D17), 4340, doi:10.1029/2001JD001151.

Bey, I., D. J. Jacob, R. M. Yantosca, J. A. Logan, B. D. Field, A. M. Fiore, Q. B. Li, H. Liu, L. J. Mickley, and M. G. Schultz (2001), Global modeling of tropospheric chemistry with assimilated meteorology: Model description and evaluation, *J. Geophys. Res., 106*, 23,073–23,095, doi:10.1029/2001JD000807.

Bhartia, P. K., R. D. McPeters, L. E. Flynn, S. Taylor, N. A. Kramarova, S. Frith, B. Fisher, and M. DeLand (2013), Solar backscatter UV (SBUV) total ozone and profile algorithm, *Atmos. Meas. Tech., 6*, 2533–2548, doi:10.5194/amt-6-2533-2013.

Bian, H., and Prather, M. J. (2002), Fast-J2: Accurate simulations of photolysis in global climate models, *J. Atmos. Chem., 41*, 281–296, doi:10.1023/A:1014980619462.

Bloom, S., L. Takacs, A. DaSilva, and D. Ledvina (1996), Data assimilation using incremental analysis updates, *Mon. Wea. Rev., 124*, 1256–1271.

Brown, S. S., et al. (2012), Effects of NOx control and plume mixing on nighttime chemical processing of plumes from coal-fired power plants, *J. Geophys. Res., 117*, D07304, doi:10.1029/2011JD016954.

Chin, M., P. Ginoux, S. Kinne, O. Torres, B. N. Holben, B. N. Duncan, R. V. Martin, J. A. Logan, A. Higurashi, T. and Nakajima (2002), Tropospheric aerosol optical thickness from the GOCART model and comparisons with satellite and sunphotometer measurements, *J. Atmos. Sci., 59*, 461–483.

Chou, M.-D. (1990), Parameterizations for the absorption of solar radiation by O_2 and CO_2 with applications to climate studies, *J. Climate, 3*, 209–217.

Chou, M.-D. (1992), A solar radiation model for use in climate studies, *J. Atmos. Sci., 49*, 762–772.

Chou, M.-D., and M. J. Suarez (1994), An efficient thermal infrared radiation parameterization for use in general circulation models, NASA Tech. Memorandum, NASA/TM-1994-104606, Vol. 3, 85 pp.

Cionni, I., V. Eyring, J. F. Lamarque, W. J. Randel, D. S. Stevenson, F. Wu, G. E. Bodeker, T. G. Shepherd, D. T. Shindell, and D. W. Waugh (2011), Ozone database in support of CMIP5 simulations: results and corresponding radiative forcing, *Atmos. Chem. Phys. Discuss., 11*, 10,875–10,933, doi:10.5194/acpd-11-10875-2011.

Colarco, P. R., A. da Silva, M. Chin, and T. Diehl (2010), On-line simulations of global aerosol distributions in the NASA GEOS-4 model and comparisons to satellite and ground-based aerosol optical depth, *J. Geophys. Res., 115*, D14207, doi:10.1029/2009JD012820.

Considine, D. B., A. R. Douglass, P. S. Connell, D. E. Kinnison, and D. A. Rotman (2000), A polar stratospheric cloud parameterization for the global modeling initiative three-dimensional model and its response to stratospheric aircraft, *J. Geophys. Res., 105*(D3), 3955–3974, 10.1029/1999JD900932.

Considine, D. B., S. R. Kawa, M. R. Schoeberl, and A. R. Douglass (2003), N_2O and NOy observations in the 1999/2000 Arctic polar vortex: Implications for transport processes in a CTM, *J. Geophys. Res., 108*(D5), 4170, doi:10.1029/2002JD002525.

Considine, D. B., D. J. Bergman, and H. Liu (2005), Sensitivity of Global Modeling Initiative chemistry and transport model simulations of radon-222 and lead-210 to input meteorological data, *Atmos. Chem. Phys., 5*, 3389–3406, doi:10.5194/acp-5-3389-2005.

Cooper, O. R., et al. (2004), A case study of transpacific warm conveyor belt transport: Influence of merging airstreams on trace gas import to North America, *J. Geophys. Res., 109*, D23S08, doi:10.1029/2003JD003624.

Douglass, A. R., R. B. Rood, S. R. Kawa, and D. J. Allen (1997), A 3D simulation of the evolution of the middle latitude winter ozone in the middle stratosphere, *J. Geophys. Res., 102*(D15), 19,217–19,232, doi:10.1029/97JD01043.

Douglass, A. R., and S. R. Kawa (1999), Contrast between 1992 and 1997 high-latitude spring Halogen Occultation Experiment observations of lower stratospheric HCl. *J. Geophys. Res., 104*, 18,739–18,754, doi:10.1029/1999JD900281.

Douglass, A. R., R. S. Stolarski, S. E. Strahan, and P. S. Connell (2004), Radicals and reservoirs in the GMI chemistry and transport model: Comparison to measurements, *J. Geophys. Res., 109*, D16302, doi:10.1029/2004JD004632.

Douglass, A. R., S. E. Strahan, L. D. Oman, and R. S. Stolarski (2014), Understanding differences in chemistry climate model projections of stratospheric ozone, *J. Geophys. Res. Atmos., 119*, 4922–4939, doi:10.1002/2013JD021159.

Duncan, B., D. Portman, I. Bey and C. Spivakovsky (2000), Parameterization of OH for efficient computation in chemical tracer models, *J. Geophys. Res., 105*, 12,259–12,262, doi:10.1029/1999JD901141.

Duncan, B. N., J. A. Logan, I. Bey, I. A. Megretskaia, R. M. Yantosca, P. C. Novelli, N. B. Jones, and C. P. Rinsland (2007), The global budget of CO, 1988-1997: source estimates and validation with a global model, *J. Geophys. Res., 112*, D22301, doi:10.1029/2007JD008459.

Duncan, B. N., and J. A. Logan (2008), Model analysis of the factors regulating the trends of carbon monoxide, 1988-1997, *Atmos. Chem. Phys., 8*, 7389–7403, doi:10.5194/acp-8-7389-2008.

Duncan, B. N., L. N. Lamsal, A. M. Thompson, Y. Yoshida, Z. Lu, D. G. Streets, M. M. Hurwitz, and K. E. Pickering (2016), A space-based, high-resolution view of notable changes in urban NOx pollution around the world (2005-2014), *J. Geophys. Res. Atmos., 121*, 976–996, doi:10.1002/2015JD024121.

Eastham, S. D., D. K. Weisenstein, and S. R. H. Barrett (2014), Development and evaluation of the unified tropospheric-stratospheric chemistry extension (UCX) for the global chemistry-transport model GEOS-Chem, *Atmos. Environ., 89*, 52–63, doi:10.1016/j.atmosenv.2014.02.001.

Elshorbany, Y. F., B. N. Duncan, S. A. Strode, J. S. Wang, and J. Kouatchou (2016), The description and validation of a computationally-efficient CH_4-CO-OH (ECCOHv1.01) chemistry module for 3-D model applications, *Geosci. Model Dev., 9*, 799–822, doi:10.5194/gmd-9-799-2016.

Eyring, V., et al. (2006), Assessment of temperature, trace species and ozone in chemistry-climate model simulations of the recent past, *J. Geophys. Res., 111*, D22308, doi:10.1029/2006JD007327.

Eyring, V., et al. (2007), Multimodel projections of stratospheric ozone in the 21st century, *J. Geophys. Res., 112*, D16303, doi:10.1029/2006JD008332.

Eyring, V., T. G. Shepherd, D. W. Waugh (Eds.) (2010), SPARC Report on the Evaluation of Chemistry-Climate Models, SPARC Report No. 5, WCRP-132, WMO/TD-No. 1526, *http://www.atmosp.physics.utoronto.ca/SPARC/ccmval_final*.

Eyring, V., et al. (2013), Overview of IGAC/SPARC Chemistry-Climate Model Initiative (CCMI) community simulations in support of upcoming ozone and climate assessments, SPARC Newsletter No. 40, p. 48–66.

Fioletov, V. E., et al. (2008), The performance of the ground-based total ozone network assessed using satellite data, *J. Geophys. Res., 113*, D14313, doi:10.1029/2008JD009809.

Fiore, A. M., F. J. Dentener, O. Wild, C. Cuvelier, M. G. Schultz, P. Hess, C. Textor, et al. (2009), Multimodel estimates of intercontinental source-receptor relationships for ozone pollution, *J. Geophys. Res., 114*, D04301, doi:10.1029/2008JD010816.

Fleming, E. L., C. H. Jackman, R. S. Stolarski, and A. R. Douglas (2011), A model study of the impact of source gas changes on the stratosphere for 1850-2100, *Atmos. Chem. Phys., 11*, 8515–8541, doi:10.5194/acp-11-8515-2011.

Flemming, J., et al. (2017), The CAMS interim reanalysis of carbon monoxide, ozone, and aerosol for 2003–2015, *Atmos. Chem. Phys., 17*, 1945–1983, doi:10.5194/acp-17-1945-2017.

Frith, S. M., N. A. Kramarova, R. S. Stolarski, R. D. McPeters, P. K. Bhartia, and G. J. Labow (2014), Recent changes in total column ozone based on the SBUV Version 8.6 Merged Ozone Data Set, *J. Geophys. Res. Atmos., 119*, 9735–9751, doi:10.1002/2014JD021889.

Garcia, R. R., and B. A. Boville (1994), Downward control of the mean meridional circulation and temperature distribution of the polar winter stratosphere, *J. Atmos. Sci., 51*, 2238–2245.

Garfinkel, C. I., A. Molod, L. D. Oman, and I.-S. Song (2011). Improvement of the GEOS-5 AGCM upon updating the air-sea roughness parameterization, *Geophys. Res. Lett., 38*, L18702, doi:10.1029/2011GL048802.

Gelaro, R., et al. (2015), Evaluation of the 7-km GEOS-5 Nature Run, NASA Tech. Rep. Series on Global Modeling and Data Assimilation, NASA/TM-2014-104606, Vol. 36, 305 pp.

Gelaro, R., et al. (2017), The Modern-Era Retrospective Analysis for Research and Applications, Version-2 (MERRA-2), *J. Climate, 30*, 5419–5454, doi:10.1175/JCLI-D-16-0758.1.

Griffies, S. M., and Co-authors (2005), Formulation of an ocean model for global climate simulations, *Ocean Science, 1*, 45–79, doi:10.5194/os-1-45-2005.

Guenther, A., B. Baugh, G. Brasseur, J. Greenberg, P. Harley, L. Klinger, D. Serca, and L. Vierling (1999), Isoprene emission estimates and uncertainties for the Central African EXPRESSO study domain, *J. Geophys. Res., 104*, 30,625–30,639, doi:10.1029/1999JD900391.

Guenther, A. C., T. Pierce, B. Lamb, P. Harley, and R. Fall (2000), Natural emissions of non-methane volatile organic compounds, carbon monoxide, and oxides of nitrogen from North America, *Atmos. Environ., 34*, 2205–2230, doi:10.1016/S1352-2310(99)00465-3.

Guenther, A., T. Karl, P. Harley, C. Wiedinmyer, P. I. Palmer, and C. Geron (2006), Estimates of global terrestrial isoprene emissions using MEGAN (Model of Emissions of Gases and Aerosols from Nature), *Atmos. Chem. Phys., 6*, 3181, 2013–3210, doi:10.5194/acp-6-3181-2006.

Haigh, J. D., and J. A. Pyle (1982), Ozone perturbation experiments in a two-dimensional circulation model, *Quart. J. R. Met. Soc., 108*, 5510–5574, doi:10.1002/qj.49710845705.

Heath, D. F., A. J. Krueger, H. A. Roeder, B. D. Henderson (1975), The solar backscatter ultraviolet and total ozone mapping spectrometer (SBUV/TOMS) for Nimbus G, *Opt. Eng., 14*, 323–331, 1975.

Helfand, H. M., and S. D. Schubert (1995), Climatology of the simulated Great Plains low-level jet and its contribution to the continental moisture budget of the United States, *J. Climate, 8*, 784–806.

Hill, C., C. DeLuca, V. Balaji, M. Suarez, and A. da Silva (2004), Architecture of the Earth System Modeling Framework, *Computing in Science and Engineering, 6*, 1, doi:10.1109/MCISE.2004.1255817.

Horowitz, L. W., J. Y. Liang, G. M. Gardner, and D. J. Jacob (1998), Export of reactive nitrogen from North America during summertime: Sensitivity to hydrocarbon chemistry, *J. Geophys. Res. Atmos., 103*(D11), 13,451–13,476, doi:10.1029/97JD03142.

Hudman, R. C., N. E. Moore, A. K. Mebust, R. V. Martin, A. R. Russell, L. C. Valin, and R. C. Cohen (2012), Steps towards a mechanistic model of global soil nitric oxide emissions: implementation and space based-constraints, *Atmos. Chem. Phys., 12*, 7779–7795, doi:10.5194/acp-12-7779-2012.

Iacono, M. J., E. J. Mlawer, S. A. Clough, and J.-J. Morcrette (2000), Impact of an improved longwave radiation model, RRTM, on the energy budget and thermodynamic properties of the NCAR community climate model, CCM3, *J. Geophys. Res., 105*(D11), 14,873–14,890, doi:10.1029/2000JD900091.

Jacob, D. J., and P. S. Bakwin (1991), Cycling of NO_x in tropical forest canopies and its implications for the global source of biogenic NO_x to the atmosphere, in Microbial Production and Consumption of Greenhouse Gases, edited by W.B. Whitman, American Society of Microbiology, Washington DC.

Jacob, D. J. and M. J. Prather (1990), Radon-222 as a test of convective transport in a general circulation model. *Tellus B, 42*, 118–134, doi: 10.1034/j.1600-0889.1990.00012.x.

Jacobson, M. Z. (1995), Computation of Global Photochemistry with SMVGEAR-II, *Atmos. Environ., 29*(18), 2541–2546, doi:10.1016/1352-2310(95)00194-4.

Jordan, C. E., J. E. Dibb, and R. C. Finkel (2003), $^{10}Be/^{7}Be$ tracer of atmospheric transport and stratosphere-troposphere exchange, *J. Geophys. Res., 108*(D8), 4234, doi:10.1029/2002JD002395.

Kawa, S. R., J. B. Kumer, A. R. Douglass, A. E. Roche, S. E. Smith, F. W. Taylor, and D. J. Allen (1995), Missing chemistry of reactive nitrogen in the upper stratospheric polar winter, *Geophys. Res. Lett., 22*, 2629–2632, doi:10.1029/95GL02336.

Kinnison, D. E., et al. (2001), The Global Model Initiative Assessment Model: Applications to high-speed civil transport perturbation, *J. Geophys. Res., 106*, 1693–1712, doi:10.1029/2000JD900406.

Kondo, J. (1975), Air-sea bulk transfer coefficients in diabatic conditions, *Boundary Layer Meteor., 9*, 91–112.

Lamsal, L. N., B. N. Duncan, Y. Yoshida, N. A. Krotkov, K. E. Pickering, D. G. Streets, Z. Lu (2015), U.S. NO_2 trends (2005-2013): EPA Air Quality System (AQS) data versus improved observations from the Ozone Monitoring Instrument (OMI), *Atmos. Env., 110*, 130–143, doi:10.1016/j.atmosenv.2015.03.055.

Large, W. G., and S. Pond (1981), Open ocean momentum flux measurements in moderate to strong winds. *J. Phys. Oceanogr., 11*, 324–336.

Lean, J. (2000), Evolution of the Sun's spectral irradiance since the Maunder Minimum, *Geophys. Res. Lett., 27*, 2425–2428.

Levelt, P. F., G. H. J. van den Oord, M. R. Dobber, A. Mälkki, H. Visser, J. de Vries, P. Stammes, J. O. V. Lundell, and H. Saari (2006), The Ozone Monitoring Instrument, *IEEE Trans. Geosci. Remote Sens., 44*, 1093–1011, doi:10.1109/TGRS.2006.872333.

Liaskos, C. E., D. J. Allen, and K. E. Pickering (2015), Sensitivity of tropical tropospheric composition to lightning NO_x production as determined by replay simulations with

GEOS-5, *J. Geophys. Res. Atmos., 120*, 8512–8534, doi:10.1002/2014JD022987.

Lin, S.-J. (2004), A vertically Lagrangian finite-volume dynamical core for global models, *Mon. Wea. Rev., 132*, 2293–2307.

Lin, S.-J., and R. B. Rood (1996), Multidimensional flux form semi-Lagrangian transport schemes, *Monthly Weather Review, 124*, 2046–2070, doi:10.1175/1520-0493(1996)124<2046:MFFSLT>2.0.CO;2.

Lin, S.-J., and R. B. Rood (1997), An explicit flux-form semi-Lagrangian shallow-water model on the sphere, *Q. J. R. Meteorol. Soc., 123*, 2477–2498, doi:10.1002/qj.49712354416.

Liu, X, P.-L. Ma, H. Wang, S. Tilmes, B. Singh, R. C. Easter, S. J. Ghan, and P. J. Rasch (2016), Description and evaluation of a new four-mode version of the Modal Aerosol Module (MAM4) within version 5.3 of the Community Atmosphere Model, *Geosci. Model Dev., 9*, 505–522, doi: 10.5194/gmd-9-505-2016.

Lock, A. P., A. R. Brown, M. R. Bush, G. M. Martin, and R. N. B. Smith (2000), A new boundary layer mixing scheme. Part I: Scheme description and single-column model tests. *Mon. Wea. Rev., 138*, 3187–3199.

Long, M. S., R. Yantosca, J. E. Nielsen, C. A. Keller, A. da Silva, M. P. Sulprizio, S. Pawson, and D. J. Jacob (2015), Development of a grid-independent GEOS-Chem chemical transport model (v9-02) as an atmospheric chemistry module for Earth system models, *Geosci. Model Dev., 8*, 595–602, doi:10.5194/gmd-8-595-2015.

Louis, J., and J. Geleyn (1982), A short history of the PBL parameterization at ECMWF. Proc. ECMWF Workshop on Planetary Boundary Layer Parameterization, Reading, United Kingdom, ECMWF, 59–80.

Manzini, E., and J. Feichter (1999), Simulation of the SF_6 tracer with the middle atmosphere MAECHAM4 model: Aspects of large-scale transport, *J. Geophys. Res., 104*, D24, 31,097–31,108, doi:10.1029/1999JD900963.

Martini, M., D. J. Allen, K. E. Pickering, G. L. Stenchikov, A. Richter, E. J. Hyer, and C. P. Loughner (2011), The impact of North American anthropogenic emissions and lightning on long-range transport of trace gases and their export from the continent during summers 2002 and 2004, *J. Geophys. Res., 116*, D07305, doi:10.1029/2010JD014305.

McGrath-Spangler, E. L., and A. Molod (2014), Comparison of GEOS-5 AGCM planetary boundary layer depths computed with various definitions, *Atmos. Chem. Phys., 14*, 6717–6727, doi:10.5194/acp-14-6717-2014.

McFarlane, N. A. (1987), The effect of orographically excited gravity-wave drag on the circulation of the lower stratosphere and troposphere, *J. Atmos. Sci., 44*, 1775–1800.

McPeters, R. D., Labow, G. J., and Logan, J. A. (2007), Ozone climatological profiles for satellite retrieval algorithms, *J. Geophys. Res., 112*, D05308, doi:10.1029/2005JD006823.

Meinshausen, M., S. J. Smith, K. Calvin, J. S. Daniel, M. L. T. Kainuma, J. F. Lamarque, K. Matsumoto, S. A. Montzka, S. C. B. Raper, K. Riahi, A. Thomson, J. G. M. Velders, and D. P. P. van Vuuren (2011), The RCP greenhouse gas concentrations and their extensions from 1765 to 2300, *Climatic Change, 109*(1-2): 213–241, doi:10.1007/s10584-011-0156-z.

Molod, A. (2012), Constraints on the total water PDF in GCMs from AIRS data and a high resolution model, *J. Climate, 25*, 8341–8352, doi: 10.1175/JCLI-D-11-00412.1.

Molod, A., L. Takacs, M. Suarez, J. Bacmeister, I.-S. Song, and A. Eichmann (2012), The GEOS-5 Atmospheric General Circulation Model: Mean Climate and Development from MERRA to Fortuna, NASA Tech. Rep. Series on Global Modeling and Data Assimilation, NASA/TM-2012-104606, Vol. 28, 117 pp.

Molod, A., G. Partyka, and M. Suarez (2013), The impact of limiting ocean roughness on GEOS-5 AGCM tropical cyclone forecasts, *Geophys. Res. Lett., 40*, 411–416, doi:10.1029/2012GL053979.

Molod, A., L. Takacs, M. Suarez, and J. Bacmeister (2015), Development of the GEOS-5 atmospheric general circulation model: evolution from MERRA to MERRA2, *Geosci. Model Dev., 8*, 1339–1356, doi:10.5194/gmd-8-1339-2015.

Moorthi, S., and M. J. Suarez (1992), Relaxed Arakawa Schubert: A parameterization of moist convection for general circulation models, *Mon. Wea. Rev., 120*, 978–1002.

Moss, R. H., et al. (2010), The next generation of scenarios for climate change research and assessment, *Nature, 463*(7282), 747–756, doi:10.1038/nature08823.

Naik, V., et al. (2013), Preindustrial to present-day changes in tropospheric hydroxyl radical and methane lifetime from the Atmospheric Chemistry and Climate Model Intercomparison Project (ACCMIP), *Atmos. Chem. Phys., 13*, 5277–5298, doi:10.5194/acp-13-5277-2013.

Newton, C. W., and A. Trevisan (1984), Clinogenesis and frontogenesis in jet-stream waves, Part I: Analytical relations to wave structure. *J. Atmos. Sci., 41*, 2717–2734.

Olson, J. (1992), World Ecosystems (WEI.4): Digital raster data on a 10-minute geographic 1080 x 2160 grid, in Global ecosystems database, version 1.0: Disc A, edited by NOAA Natl. Geophys. Data Center, Boulder, Colorado.

Oman, L. D., and A. R. Douglass (2014), Improvements in total column ozone in GEOSCCM and comparisons with a new ozone-depleting substances scenario, *J. Geophys. Res. Atmos., 119*, 5613–5624, doi:10.1002/2014JD021590.

Orbe, C., D. W. Waugh, and P. A.Newman (2015), Air-mass origin in the tropical lower stratosphere: The influence of Asian boundary layer air, *Geophys. Res. Lett., 42*, doi:10.1002/2015GL063937.

Ott, L. E., B. N. Duncan, A. M. Thompson, G. Diskin, Z. Fasnacht, A. O. Langford, M. Lin, A. M. Molod, J. E. Nielsen, S. E. Pusede, K. Wargan, A. J. Weinheimer, Y. Yoshida (2016), Frequency and impact of summertime stratospheric intrusions over Maryland during DISCOVER-AQ (2011): New evidence from NASA's GEOS-5 simulations, *J. Geophys. Res., 121*, 3687–3706, doi:10.1002/2015JD024052.

Patra, P. K., S. Houweling, M. Krol, P. Bousquet, D. Belikov, D. Bergmann, H. Bian, P. Cameron-Smith, M. P. Chipperfield, K. Corbin, A. Fortems-Cheiney, A. Fraser, E. Gloor, P. Hess, A. Ito, S. R. Kawa, R. M. Law, Z. Loh, S. Maksyutov, L. Meng, P. I. Palmer, R. G. Prinn, M. Rigby, R. Saito, and C. Wilson (2011), TransCom model simulations of CH_4 and related species: linking transport, surface flux and chemical loss with CH_4 variability in the troposphere and lower stratosphere, *Atmos. Chem. Phys., 11*, 12,813-12,837, doi:10.5194/acp-11-12813-2011.

Pawson, S., I. Stajner, S. R. Kawa, H. Hayashi, W. Tan, J. E. Nielsen, Z. Zhu, L.-P. Chang, N. J. Livesey (2007), Stratospheric transport using six-hour averaged winds from a data assimilation system. *J. Geophys. Res., 112*, D23103, doi:10.1029/2006JD007673.

Pawson, S., R. S. Stolarski, A. R. Douglass, P. A. Newman, J. E. Nielsen, S. M. Frith, and M. L. Gupta (2008), Goddard Earth Observing System Chemistry-Climate Model simulations of stratospheric ozone-temperature coupling between 1950 and 2005, *J. Geophys. Res., 113*, D12103, doi:10.1029/2007JD009511.

Perlwitz, J., S. Pawson, R. L. Fogt, J. E. Nielsen, and W. D. Neff (2008), Impact of stratospheric ozone hole recovery on Antarctic climate, *Geophys. Res. Lett., 35*, L08714, doi:10.1029/2008GL033317.

Prather, M. J., and C. M. Spivakovsky (2009), Tropospheric OH and the lifetimes of hydrochlorofluorocarbons, *J. Geophys. Res., 95*, 18,723–18,729, doi:10.1029/JD095iD11p18723.

Prather, M. J., X. Zhu, Q. Tang, J. Hsu, and J. L. Neu (2011), An atmospheric chemist in search of the tropopause, *J. Geophys. Res., 116*, D04306, doi:10.1029/2010JD014939.

Putman, W. M., and S.-J. Lin (2007), Finite-volume transport on various cubed-sphere grids, *J. Comp. Phys., 227*, 55–78, doi:10.1016/j.jcp.2007.07.022.

Putman, W. M., and M. Suarez (2011), Cloud-system resolving simulations with the NASA Goddard Earth Observing System global atmospheric model (GEOS-5), *Geophys. Res. Lett., 38*, L16809, doi:10.1029/2011GL048438.

Rienecker, M. M., et al. (2008), The GEOS-5 Data Assimilation System: Documentation of versions 5.0.1 and 5.1.0, and 5.2.0, NASA Tech. Rep. Series on Global Modeling and Data Assimilation, NASA/TM-2008-104606, Vol. 27, 92 pp.

Rienecker, M. M., et al. (2011), MERRA: NASA's Modern-Era Retrospective Analysis for Research and Applications, *J. Climate, 24*, 1–25, doi:10.1175/JCLI-D-11-00015.1.

Santee, M. L., I. A. MacKenzie, G. L. Manney, M. P. Chipperfield, P. F. Bernath, K. A. Walker, C. D. Boone, L. Froidevaux, N. J. Livesey and J. W. Waters (2008), A study of stratospheric chlorine partitioning based on new satellite measurements and modeling, *J. Geophys. Res., 113*, D12307, doi:10.1029/2007JD009057.

Schubert, S. D., H. Wang, R. D. Koster, M. J. Suarez and P. Y. Groisman (2014), Northern Eurasian heat waves and droughts, *J. Climate, 27*, 3169–3207, doi:10.1175/JCLI-D-13-00360.1.

Shindell, D. T., et al. (2006), Multimodel simulations of carbon monoxide: Comparison with observations and projected near-future changes, *J. Geophys. Res., 111*, D19306, doi:10.1029/2006JD007100.

Shindell, D. T., et al. (2008), A multi-model assessment of pollution transport to the Arctic, *Atmos. Chem. Phys., 8*, 5353–5372, doi:10.5194/acp-8-5353-2008.

Simmons, A. J., and D. M. Burridge (1981), An energy and angular-momentum conserving vertical finite-difference scheme and hybrid vertical coordinates, *Mon. Wea. Rev., 109*, 758–766.

Spivakovsky, C, S. Wofsy, and M. Prather (1990a), A numerical method for the parameterization of atmospheric chemistry: Computation of tropospheric OH, *J. Geophys. Res., 95*, 18,433–18,439, doi:10.1029/JD095iD11p18433.

Spivakovsky, C. M., R. Yevich, J. A. Logan, S. C. Wofsy, M. B. McElroy, and M. J. Prather, (1990b), Tropospheric OH in a three-dimensional chemical tracer model: An assessment based on observations of CH_3CCl_3, *J. Geophys. Res., 95*, 18,441–18,471, doi:10.1029/JD095iD11p18441.

Spivakovsky, C. M., J. A. Logan, S. A. Montzka, Y. J. Balkanski, M. Foreman-Fowler, D. B. A. Jones, L. W. Horowitz, A. C. Fusco, C. A. M. Brenninkmeijer, M. J. Prather, S. C. Wofsy, and M. B. McElroy (2000), Three-dimensional climatological distribution of tropospheric OH: Update and evaluation, *J. Geophys. Res., 105*, 8931–8980, doi:10.1029/1999JD901006.

Stohl, A., S. Eckhardt, C. Forster, P. James, and N. Spichtinger (2002), On the pathways and timescales of intercontinental air pollution transport, *J. Geophys. Res., 107*(D23), 4684, doi:10.1029/2001JD001396.

Stolarski, R. S., A. R. Douglass, P. A. Newman, S. Pawson, and M. R. Schoeberl (2010), Relative contribution of greenhouse gases and ozone-depleting substances to temperature trends in the stratosphere: A chemistry-climate model study, *J. Climate, 23*, 28–42, doi:10.1175/2009JCLI2955.1.

Stolarski, R. S., A. R. Douglass, M. Gupta, P. A. Newman, S. Pawson, M. R. Schoeberl, and J. E. Nielsen (2006), An ozone increase in the Antarctic summer stratosphere: A dynamical response to the ozone hole, *Geophys. Res. Lett., 33*, L21805. doi:10.1029/2006GL026820.

Strahan, S. E., A. R. Douglass, and P. A. Newman (2013), The contributions of chemistry and transport to low arctic ozone in March 2011 derived from Aura MLS observations, *J. Geophys. Res. Atmos., 118*, 1563–1576, doi:10.1002/jgrd.50181.

Strode, S. A., J. M. Rodriguez, J. A. Logan, O. R. Cooper, J. C. Witte, L. N. Lamsal, M. Damon, B. Van Aartsen, S. D. Steenrod, and S. E. Strahan (2015), Trends and Variability in Regional Surface Ozone over the United States, *J. Geophys. Res. Atmos., 120*, 9020–9042, doi:10.1002/2014JD022784.

Suarez, M., A. Trayanov, C. Hill. P. Schopf, and Y. Vikhliaev (2007), MAPL: A high-level programming paradigm to support more rapid and robust encoding of hierarchical trees of interacting high-performance components, Proceedings of the 2007 Symposium on Component and Framework Technology in High-Performance and Scientific Computing, pp. 11–20, doi:10.1145/1297385.1297388.

Swartz, W. H., R. S. Stolarski, L. D. Oman, E. L. Fleming, and C. H. Jackman (2012), Middle atmosphere response to different descriptions of the 11-yr solar cycle in spectral irradi-

ance in a chemistry-climate model, *Atmos. Chem. Phys., 12*, 5937–5948, doi:10.5194/acp-12-5937-2012.

Thomas, J. L., J. C. Raut, K. S. Law, L. Marelle, G. Ancellet, F. Ravetta, J. D. Fast, G. Pfister, L. K. Emmons, G. S. Diskin, A. Weinheimer, A. Roiger, and H. Schlager, (2013), Pollution transport from North America to Greenland during summer 2008, *Atmos. Chem. Phys., 13*, 3825-3848, doi:10.5194/acp-13-3825-2013.

Tokioka, T., K. Yamazaki, A. Kitoh and T. Ose (1988), The equatorial 30-60 day oscillation and the Arakawa-Schubert penetrative cumulus parameterization, *J. Meteorol. Soc. Japan, 66*, 883–901.

Velders, G. J. M. and J. S. Daniel (2014), Uncertainty analysis of projections of ozone-depleting substances: mixing ratios, EESC, ODPs, and GWPs, *Atmos. Chem. Phys., 14*, 2757–2776, doi:10.5194/acp-14-2757-2014.

Vinken, G. C. M., K. F. Boersma, J. D. Maasakkers, M. Adon, and R. V. Martin (2014), Worldwide biogenic soil NO_x emissions inferred from OMI NO_2 observations, *Atmos. Chem. Phys., 14*, 10,363–10,381, doi:10.5194/acp-14-10363-2014.

Voulgarakis, A., et al. (2013), Analysis of present day and future OH and methane lifetime in the ACCMIP simulations, *Atmos. Chem. Phys., 13*, 2563–2587, doi: 10.5194/acp-13-2563-2013.

Wargan, K., S. Pawson, M. A. Olsen, J. C. Witte, A. R. Douglass, J. R. Ziemke, S. E. Strahan, and J. E. Nielsen (2015), The global structure of upper troposphere-lower stratosphere ozone in GEOS-5: A multiyear assimilation of EOS Aura data, *J. Geophys. Res. Atmos., 120*, 201–2036, doi:10.1002/2014JD022493.

Waters, J., et al. (2006), The Earth Observing System Microwave Limb Sounder (EOS MLS) on the Aura satellite, *IEEE Trans. Geosci. Remote Sens., 44*, 1075–1092, doi:10.1109/TGRS.2006.873771.

Waugh, D. W. and Eyring, V. (2008), Quantitative performance metrics for stratospheric–resolving chemistry–climate models, *Atmos. Chem. Phys., 8*, 5699–5713, doi:10.5194/acp-8-5699-2008.

Waugh, D. W., and T. M. Hall (2002), Age of stratospheric air: Theory, observations, and models, *Rev. Geophys., 40*, no. 4, 1010, doi:10.1029/2000RG000101.

Wild, O., Q. Zhu, and M. J. Prather (2000), Fast-J: Accurate simulation of in- and below-cloud photolysis in global chemical models, *J. Atmos. Chem., 37*, 245–282, doi:10.1023/A:1006415919030.

World Meteorological Organization (2011), Scientific Assessment of Ozone Depletion: 2010, Global Ozone Research and Monitoring Project – Report No. 52, 516 pp., Geneva, Switz.

World Meteorological Organization (WMO), Scientific Assessment of Ozone Depletion: 2014, Global Ozone Research and Monitoring Project – Report No. 55, 416 pp., Geneva, Switz.

Wu, W.-S., R.J. Purser and D.F. Parrish (2002), Three-dimensional variational analysis with spatially inhomogeneous covariances, *Mon. Wea. Rev., 130*, 2905–2916.

Yienger, J. J., and H. Levy II (1995), Empirical model of global soil-biogenic NO_x emissions, *J. Geophys. Res., 100*(D6), 11,447–11,464, doi:10.1029/95JD00370.

Ziemke, J. R., S. Chandra, G. Labow, et al. (2011), A global climatology of tropospheric and stratospheric ozone derived from Aura OMI and MLS measurements, *Atmos. Chem. Phys., 11*, 9237–9251, doi:10.5194/acp-11-9237-2011.